Volume 18
DOE/DP40124-42

LLE Review

Quarterly Report

January–March 1984

Laboratory for Laser Energetics
College of Engineering and Applied Science
University of Rochester
250 East River Road
Rochester, New York 14623

Volume 18
DOE/DP40124-42

LLE Review

Quarterly Report

Editor: L. Lund
(716) 275-4781

January–March 1984

Laboratory for Laser Energetics
College of Engineering and Applied Science
University of Rochester
250 East River Road
Rochester, New York 14623

This report was prepared as an account of work conducted by the Laboratory for Laser Energetics and sponsored by Empire State Electric Energy Research Corporation, General Electric Company, New York State Energy Research and Development Authority, Northeast Utilities Service Company, Southern California Edison Company, The Standard Oil Company, University of Rochester, the U.S. Department of Energy, and other United States government agencies.

IN BRIEF

This volume of the LLE Review contains articles on the operations of the GDL and OMEGA facilities, energy measurement and beam characterization in the ultraviolet (UV), theoretical calculations of thermal self-focusing in laser plasmas, two aspects of the picosecond optics activities at the LLE, and the NLUF activities during this quarter (January through March 1984).

Highlights of these articles include the following:

- The OMEGA energy measurement system for the UV has shown an improved measurement consistency of 1% rms, and a photodiode system has been activated to measure the 1ω, 2ω, and 3ω output from the frequency-conversion crystals. The diodes are currently consistent to $\pm$ 3% rms.
- Holography has been demonstrated as a potential method of characterizing the near field and equivalent-target-plane intensity distributions as well as the phase front of the pulsed UV output of GDL and OMEGA.
- Hydrodynamic simulations of thermal self-focusing in laser-generated plasmas have been carried out in order to understand the basic scaling of this effect.
- A time-dependent semiclassical theory of gain-coupled distributed feedback lasers (DFL) has been developed and simulations of a dye DFL have been done.

- The shaping of electrical transients in microstriplines has been extended to the nanosecond regime which is of interest for optical pulse-shaping for inertial fusion.

In addition, Southern California Edison has signed on as a new industrial sponsor of the Laser Fusion Feasibility Project (LFFP) at the LLE. This addition of a west coast utility as a sponsor highlights the national scope of the inertial fusion effort at the LLE.

CONTENTS

		Page
IN BRIEF		iii
CONTENTS		v
Section 1	LASER SYSTEM REPORT	53
1.A	GDL Facility Report	53
1.B	OMEGA Facility Report	54
Section 2	PROGRESS IN LASER FUSION	56
2.A	OMEGA Energy Measurement	56
2.B	Holographic Wavefront Measurement of the GDL Frequency-Converted Laser Beam	61
2.C	Hydrodynamic Simulations of Thermal Self-Focusing in Laser-Generated Plasmas	72
Section 3	ADVANCED TECHNOLOGY DEVELOPMENTS	84
3.A	Time-Dependent Semiclassical Theory of Gain-Coupled Distributed Feedback Lasers	84
3.B	Pulse Shaping with Dispersive Microstriplines	93
Section 4	NATIONAL LASER USERS FACILITY NEWS	99
PUBLICATIONS		

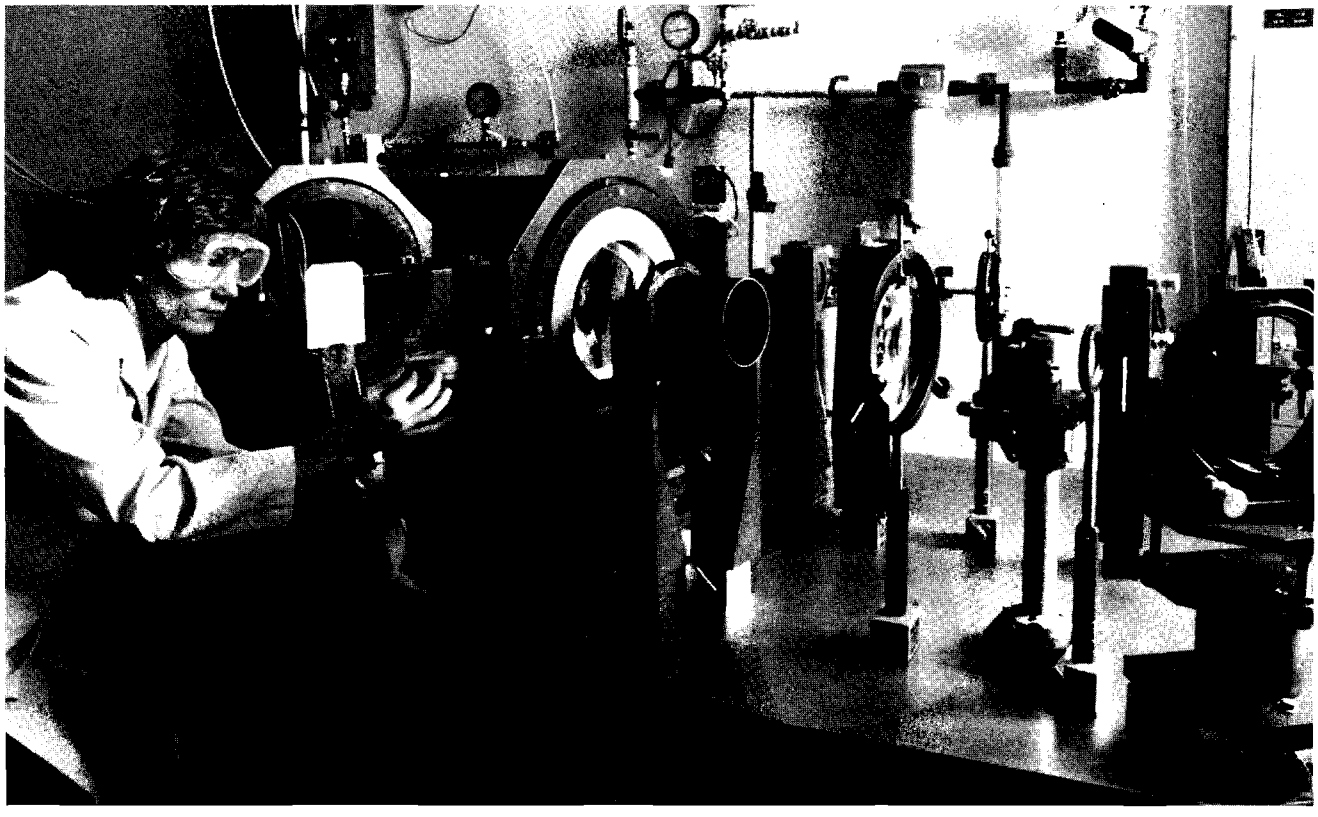

Terrance Kessler, a research engineer in the Engineering Division, is shown adjusting the holographic beam-characterization setup used on the 351-nm GDL system. This apparatus has been used to provide intensity and phase information on the pulsed beam. See the article in this volume for more information on this technique.

Section 1
LASER SYSTEM REPORT

1.A GDL Facility Report

The glass development laser (GDL) system continued activity this quarter as a UV interaction facility. Shots were taken in support of various interaction programs, transport studies, users, and damage testing. A highlight of the quarter was a record-breaking 102 target shots in a single week in support of damage testing.

A summary of shots on GDL this quarter follows:

Interaction	57
X-Ray	44
Damage Testing	301
Test, Pointing, Software	34
TOTAL	436

ACKNOWLEDGMENT

This work was supported by the U.S. Department of Energy Office of Inertial Fusion under contract number DE-AC08-80DP40124 and by the Laser Fusion Feasibility Project at the Laboratory for Laser Energetics which has the following sponsors: Empire State Electric Energy Research Corporation, General Electric Company, New York State Energy Research and Development Authority, Northeast Utilities Service Company, Southern California Edison Company, The Standard Oil Company, and University of Rochester. Such support does not imply endorsement of the content by any of the above parties.

1.B OMEGA Facility Report

OMEGA system activities this quarter have consisted of normal target shooting, calibration of the energy-measurement system, and system maintenance. Members of the operations group have begun procurement activities for the frequency conversion of the next six beams of the OMEGA laser system.

The beginning of the quarter was marked by the complete calibration of the energy-measurement system, including a cross calibration of the blue output, using 8″ calorimeters with Corning 5834 UV bandpass filters. Following this calibration activity a number of experimental campaigns were carried out, including uniformity, transport (including time-resolved transport), coronal physics, and a National Laser Users Facility (NLUF) experiment from the Naval Research Laboratory. As part of the uniformity campaign, an extensive series of equivalent-target-plane (ETP) photographs was taken to characterize each of the six blue beams of OMEGA. During the uniformity series, an experiment to correlate the equivalent-target-plane UV image with the x-ray emission photograph of that beam on a large solid target was successfully attempted. Results of these tests will be published in a future report.

With the removal of the Pockels cells from the blue beams during the previous quarter, and the addition of the neutral solution lens in the output spatial filter, higher energies could be propagated through the system. The highest energy output of the system, in the UV, was 420 J, with a high beam of 95 J. Beam balance for this quarter's target shots has been consistently below 10%, with a best of 5%.

As has been the rule for the last several quarters, system performance and reliability have been keynotes of all the campaigns. Not a single day of shooting has been lost due to equipment malfunction.

In the target area, several new diagnostics have been activitated during this quarter. A photomultiplier with a sensitivity at 2ω (175 nm) was activated during the coronal physics campaign. An imaging streak camera and a streaked elliptical crystal x-ray spectrograph built at the University of Hawaii as part of an NLUF collaboration were being activated during the quarter. In addition, a backlighting target positioner and auxiliary viewing system were activated.

Additional activities of the operations group during this quarter have been the engineering of driver upgrades for OMEGA and GDL, and the continued development of the active mode-locked, Q-switched oscillators. Procurement activities by the group have resulted in the majority of the component parts for the pending frequency conversion of the six-beam "A" group of OMEGA being on order as of this writing. An exception was the new conversion cell mount, which was redesigned during this quarter.

A summary of shots on OMEGA this quarter follows:

Target Shots	156
Driver Testing	68
Beamline Test, ETP	107
Software Testing	40
TOTAL	371

ACKNOWLEDGMENT

This work was supported by the U.S. Department of Energy Office of Inertial Fusion under contract number DE-AC08-80DP40124 and by the Laser Fusion Feasibility Project at the Laboratory for Laser Energetics which has the following sponsors: Empire State Electric Energy Research Corporation, General Electric Company, New York State Energy Research and Development Authority, Northeast Utilities Service Company, Southern California Edison Company, The Standard Oil Company, and University of Rochester. Such support does not imply endorsement of the content by any of the above parties.

Section 2
PROGRESS IN LASER FUSION

2.A OMEGA Energy Measurement

Maintaining beam balance, i.e., the equality of on-target energy in each of OMEGA's beams, to within 1% rms is one of the major requirements for illumination uniformity.[1] Provision for balancing beam energies was incorporated into the system design during the construction of OMEGA. Half- and quarter-wave plates are located at most of the dielectric-coated beam splitters and at all of the polarizers in the beamline. With these waveplates, we adjust the polarization of the beams to vary the ratio of transmitted to reflected energy at the beam splitters or to reject some of the energy at the polarizers. Thus, energy is either redistributed among the beams or simply dumped. A computerized beam-balance procedure uses measured beam energies and current wave-plate settings as input data and calculates new wave-plate settings to improve the balance of beam energies. The principal limit to precise beam balance is the accuracy of the individual beam energy measurement.

Energy Measurement at 1054 nm

Our attempts over the last two years to maintain balanced beam energies resulted in 5–10% rms balance on routine shots. Random 5% fluctuations in the relative individual beam energies occurred on a shot-to-shot basis and within a few weeks, the beam balance drifted 15–20%, necessitating energy rebalance. As we addressed the problem of precise beam balance, it became clear that some of the fluctuations were due to noise and drift in the energy measurement system. The first necessary step was to characterize the beam-

energy measurement system and determine if the relative energy of the beams could be measured to within 1%.

The primary instruments for measuring laser energy are volume-absorbing calorimeters which use a thermoelectric element to convert the thermal signal to an electrical signal.[2] The response of the calorimeter is proportional to the energy in a laser pulse. Detection sensitivity is determined with calibrated electrical pulses heating an internal heater winding in the calorimeter.

The technique for measuring laser energy during a target shot consists of diverting a small fraction of the beam energy to a calorimeter. Main beam energy is the product of a calibration coefficient and the sample energy measured by the calorimeter. Calibration is carried out by firing the whole beam into a large-aperture (8") calorimeter which has been set up temporarily in the beam path. The calibration coefficient is then determined as the ratio of measured whole-beam energy to sample energy. The optical configuration for calibration of OMEGA at 1054 nm is illustrated in Fig. 18.1. Approximately 1% of the incident laser pulse is transmitted through the end mirror into the beam-diagnostic package (BDP). About 80% of the BDP input energy is sampled by a 1"-aperture

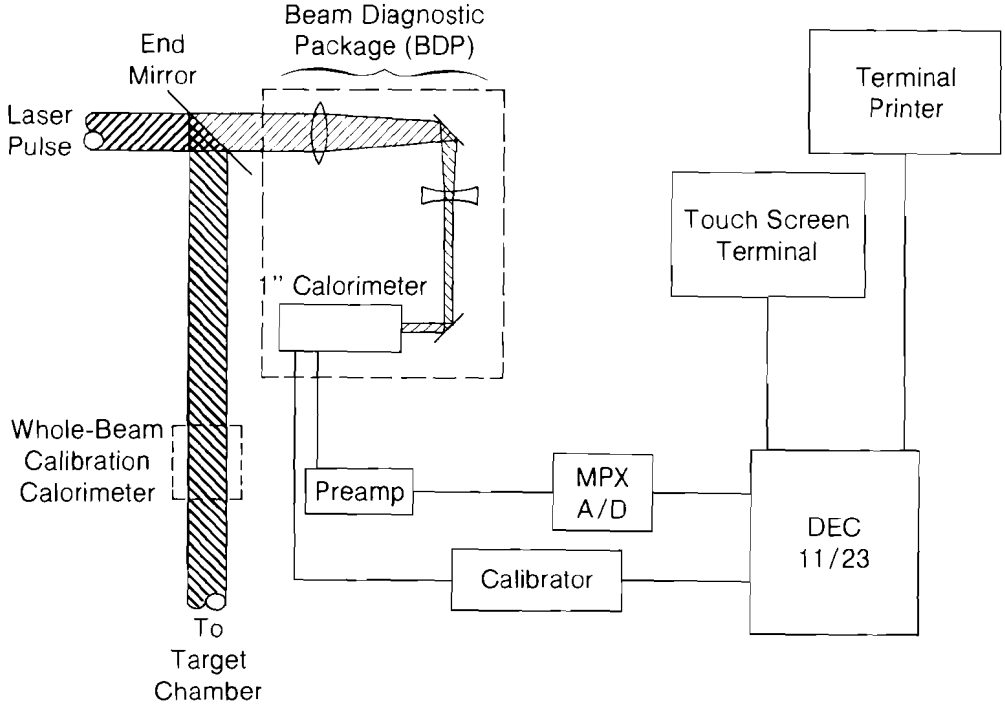

Fig. 18.1
Schematic of the OMEGA energy measurement system for 1054 nm. A small fraction (~ 1%) of the laser beam is transmitted through the end mirror to the beam-diagnostic package (BDP), and approximately 80% of this energy is measured by the 1" calorimeter. The system is calibrated by placing an 8" calorimeter in the beam after the end mirror.

calorimeter. The 8″ calorimeter is set up immediately after the end mirror for calibration. Figure 18.1 also depicts the other major elements of the OMEGA laser-energy measurement system. The low-level calorimeter output is amplified and transmitted to a minicomputer via a multiplexed A/D converter. Reduced data are summarized in a report on the terminal printer and stored on disc along with the acquired data. The same computer also fires the electrical calibrator on command for calorimeter calibration and system checkout.

The precise measurement of laser energy depends on the reliability of the 8″ reference calorimeters. Thus, the first task in the beam-balance investigation was to measure the reading consistency and the relative optical sensitivities of the 8″ calorimeters. In a special test series, the 8″ calorimeters were set up and exchanged in a systematic fashion among OMEGA beams. The following are the results of a careful analysis of the 8″ and 1″ calorimeter data from these tests.

(a) Measured optical sensitivities of the 8″ calorimeters differed from their measured electrical sensitivities, by as much as 4%.

(b) Shot-to-shot fluctuation of the energy ratios of paired calorimeters in the same beam or in different beams was about 5% rms.

(c) Relative optical sensitivity appeared to be a function of the beam energy in some cases (insufficient data for quantitative statistics).

We identified two principal causes of the random variability. First, an oscilloscope on the A/D input terminals revealed that the slow calorimeter signals were superimposed on high-frequency noise. The source of some of this noise was traced to the adjacent computers and switching-mode power supplies. This common-mode noise should have been rejected by the A/D, but was not. After concluding that this was an inadequacy in the design of the A/D converter rather than a malfunction, we replaced the A/D converters with those of another manufacturer. The second source was long-term thermal drift due to local air circulation at the calorimeter. Thoroughly insulating the calorimeter and adding a close-fitting input window eliminated this problem.

In addition, we began to suspect that the non-constant sensitivity might be an effect of the end-mirror coatings. These high-reflectivity (HR) coatings transmit about 1% of the "P" polarization and much less of the "S" component. Therefore, very small variations in reflectivity represent very large variations in transmission (e.g., a 1% decrease in reflectivity is a 100% increase in transmission for a 99% reflective coating). Initially, we thought that water vapor might be affecting the transmissivity of the coatings. However, upon investigation of the effect of ambient humidity, we concluded that this effect was negligible. This did not rule out coating effects because spatial variations in coating transmissivity could cause the energy fraction reaching the calorimeter to vary as the beam profile or the beam alignment was changed.

Energy Measurement at 351 nm

Further characterization of the energy measurement system was deferred until the first six beams of OMEGA were converted to UV. New A/D converters and repackaged 8" calorimeters (with windows and improved insulation) were designed into the UV energy measurement system to minimize the effects of the identified noise and drift sources. The calorimetry system has been retested in the same manner used at 1054 nm and a measurement consistency of 1% rms has been measured, thus confirming the elimination of the major drift and noise sources.

Energy diagnostics of frequency-tripled beams present some new challenges. Figure 18.2 illustrates the final configuration of the UV energy measurement system. A beam splitter was installed, at a low angle of incidence, in the beam between the last spatial filter and the conversion cell. The 4% reflection from the uncoated first surface is measured by a dedicated 8" calorimeter. The second surface is antireflection (AR) coated to minimize the insertion loss of the pickoff. The combination of an uncoated surface and the low angle of incidence was used to minimize any effect of beam profile change or beam misalignment. Considerations of available space, alignment stability, optical sensitivity, and cost per channel led us to specify an array of three photodiode detectors for the conversion-cell output measurements. The photodiodes we selected have fast response and excellent sensitivity and linearity at the three wavelengths of

Fig. 18.2
Schematic of the OMEGA energy measurement system for 351 nm. Energy pickoffs operate at small angles of incidence and use uncoated first surfaces and antireflection (AR)-coated second surfaces. The conversion-cell output energy at 1ω, 2ω, and 3ω is measured with photodiodes mounted in an integrating sphere. Full-aperture, 8" calorimeters are used to measure the incident 1ω beam and to cross-check the diodes. Separate 8" calorimeters are inserted in the beam to calibrate the system. Energy transport to the target is measured by inserting a 351-nm bandpass-filtered calorimeter in the beam in front of the focusing lens.

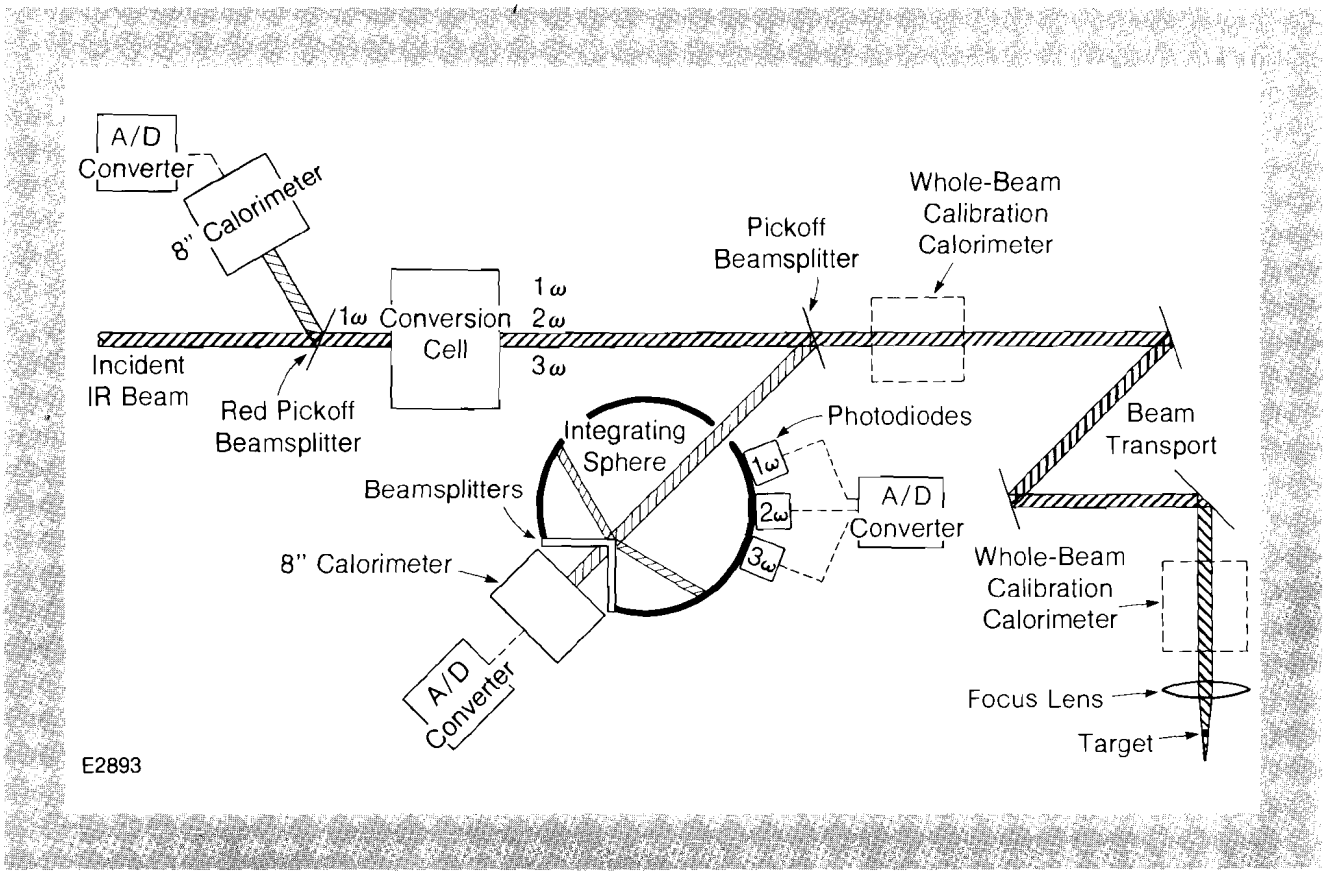

interest. These properties were confirmed in laboratory tests at LLE as part of the system design procedure. The three photodiodes are mounted on the surface of an integrating sphere, and appropriate filter stacks in front of each diode select one of the three output harmonics and attenuate the optical signal. The input to the integrating sphere is another Fresnel reflection from a fused-silica beam splitter in the conversion-cell output beam. This diagnostic beam enters the integrating sphere through a baffled input aperture to minimize stray-light noise. At the back of the sphere the beam strikes a wedged fused-silica beam splitter which reflects 8% of the light onto the diffusing inner surface and transmits 92% of the light to an unfiltered 8″ calorimeter. The integrating-sphere calorimeter measurement is a check on the energy sum of the diode channels, and it provides a backup in case one of the three diode channels should fail.

We calibrate the MESS (Multi-Wavelength Energy-Sensing System) against the response of an 8″ calorimeter set up temporarily in the main beam following the MESS pickoff as shown in Fig. 18.2. First, the tripling cell is detuned to minimize harmonic conversion, then the cell is tuned to generate 2ω light, and then the tripler is tuned for maximum 3ω generation. Simple linear regression analysis yields the diode calibration coefficients in joules/count. UV diode calibrations are rechecked from time to time with an 8″ calorimeter fitted with a UV transmitting filter. We selected the diodes and designed the system for less than 1% rms measurement consistency; however, the UV diodes are currently calibrated to ±3% rms at full OMEGA output. Further measurements of the diode subsystem are in progress. The UV calorimeter assembly is also set up at the final focus lens to measure the transmission from the MESS pickoff to the target (see Fig. 18.2). This is required for accurate measurement of the UV energy on target.

Summary

Experience with the revised and augmented energy measurement system has been encouraging. Eight-inch calorimeter statistics demonstrate a consistency of 1% or better measurement accuracy for fixed output energy. There is some indication, however, that optical sensitivity may be a weak function of energy. We have designed a precision electrical calibrator to enable us to determine the absolute sensitivity of the calorimeters as a function of deposited energy over a range of 1 to 100 J. This device will help resolve this question of linearity. The photodiode subsystem, totally new in OMEGA, is rapidly attaining full operational status, although it has not reached the 1% rms precision required. Confirmation of improved diode precision is still pending, but we are confident that we can perfect this subsystem.

ACKNOWLEDGMENT

This work was supported by the U.S. Department of Energy Office of Inertial Fusion under contract number DE-AC08-80DP40124 and by the Laser Fusion Feasibility Project at the Laboratory for Laser Energetics which has the following sponsors: Empire State Electric Energy Research Corporation, General Electric Company, New York State Energy Research and Development Authority, Northeast Utilities Service

Company, Southern California Edison Company, The Standard Oil Company, and University of Rochester. Such support does not imply endorsement of the content by any of the above parties.

REFERENCES

1. S. Skupsky and K. Lee, *J. Appl. Phys.* **54**, 3662 (1983).

2. S. R. Gunn, *J. Phys. E* **6**, 105 (1973).

2.B Holographic Wave-Front Measurement of the GDL Frequency-Converted Laser Beam

One of the current objectives of the uniformity activity at the LLE is to determine the factors which control the quasi-far-field intensity distribution of the individual frequency-converted laser beams and to determine the extent to which these factors can be manipulated to optimize overall irradiation uniformity on a target.[1] Measurement techniques, which generate near-field intensity and phase distributions, as well as quasi-far-field intensity distributions of individual laser beams, are essential in fulfilling these objectives. Holographic wavefront measurement is capable of recording all of the information necessary for the complete recovery of the original complex amplitude distribution. Holographically generated near-field intensity and phase profiles, together with a two-dimensional (2-D) beam propagation code, constitute a predictive tool for the calculation of the quasi-far-field intensity distribution at any given target plane.[2] Furthermore, computer-based amplitude and phase modulation studies could be performed with the use of this predictive tool, and experimental corroboration would be possible with a continuum of cw, holographically reconstructed, quasi-far-field profiles of the pulsed laser beam.

Conventional Wave-Front Measurement

Wave-front-measurement techniques, previously used at 1054 nm, were redesigned for use on the GDL frequency-tripled laser beam as shown in Fig. 18.3. GDL is characterized by the following parameters:

Wavelength	351 nm
Energy	0-70 J
Pulse Width	850 ps (FWHM)
Diameter	125 mm
Polarization	linear, vertical

The first path transports the beam through a focusing lens and into an equivalent-target-plane (ETP) camera. The focusing beam is injected into a 1° wedged beam splitter (reflectivity = 70% both surfaces), thus producing both a transmitted and a reflected one-dimensional (1-D) array in exposure. The reflected array contains several images which differ in intensity by one-half. The intensity of the first image is larger than the others in order to check for the high-intensity photographic errors characteristic of a limited dynamic

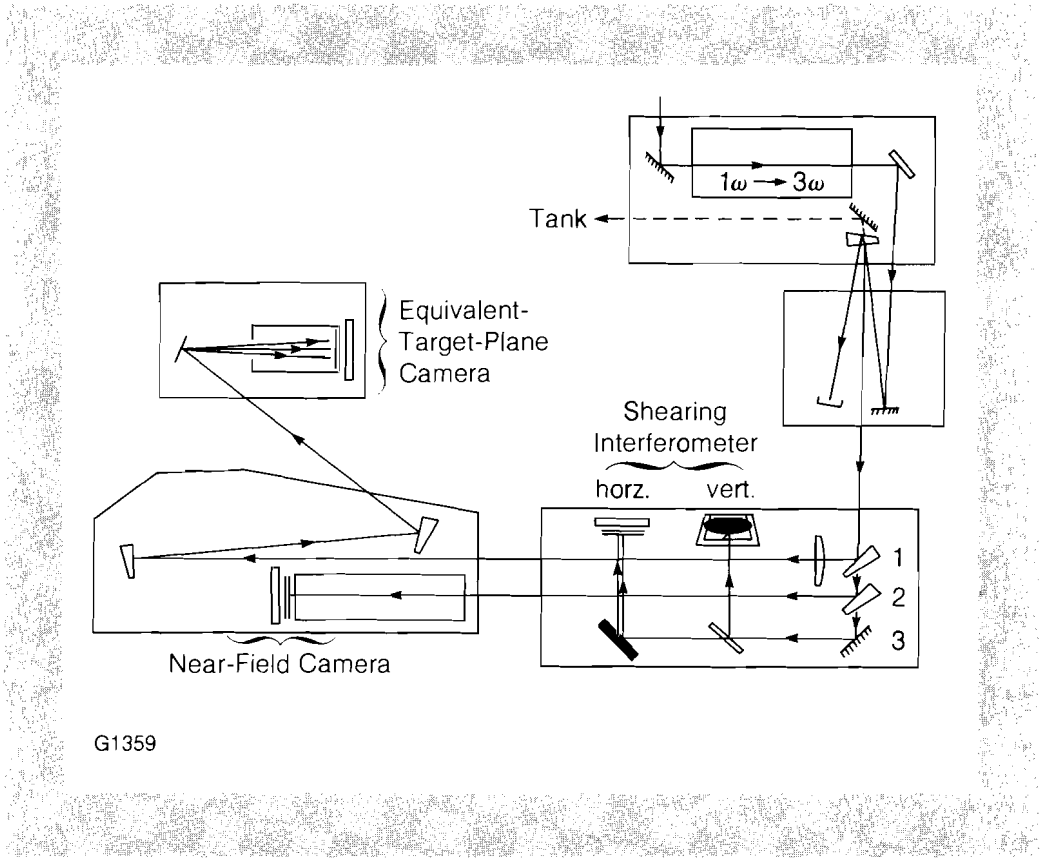

Fig. 18.3
The conventional experimental setup includes a near-field (NF) camera, an equivalent-target-plane (ETP) camera, and a lateral-shearing interferometer with two orthogonally oriented shear plates.

range in the recording medium. The second path directed the beam into a near-field camera, while the third path was used for lateral-shearing interferometry. The two slightly wedged plates, orthogonally oriented, shear the laser beam to produce fringes that represent loci of constant wave-front slope.

These wave-front-measurement techniques provided a good characterization of the GDL frequency-converted laser beam. Figure 18.4 shows the photographic result of a 1-D ETP array, a near-field photograph, and horizontal and vertical lateral-shearing interferograms. Defects in the conversion crystals were located, and distortions in the crystal cell were found. The equivalent target plane, representing tangential focus, was accurately recorded without image distortion. A quantitative analysis of the interferogram was not performed, since a visual inspection clearly indicated a severe aberration problem in the beam. A subsequent interferometric study of the frequency-conversion crystals and crystal cells determined that they were the source of most of the phase error. However, the lateral-shearing interferometry does not record the phase front of the beam in a form which is easy to interpret. The equivalent-target-plane camera has not been proved to be successful at the exact focus of the lens. A holographic technique is capable of producing both a 2-D map of the phase front, and a continuum of ETP images that approach the focal plane, thus offering interferometric and intensity-measurement capabilities not presently available for pulsed-beam analysis.

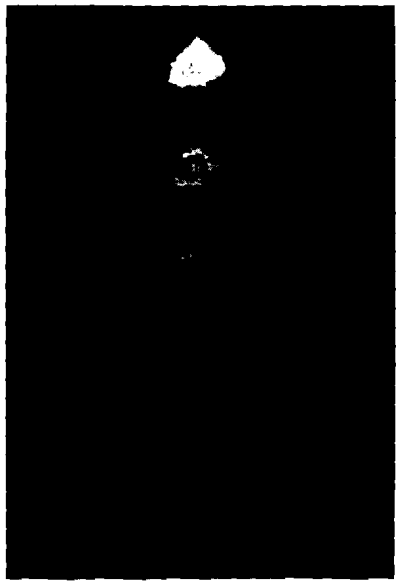

Equivalent-Target-Plane
Array (true size)

0 (mm) 125
Near Field

Vertical Shear

Horizontal Shear

G1338

Fig. 18.4
The photographic results of the conventional wave-front-measurement techniques include a 1-D ETP array in exposure, a near-field image, and two orthogonally oriented shearing interference patterns.

Holographic Wave-Front Recording and Reconstruction

Holography is a method of recording and reconstructing the complex amplitude of a wave front. This is achieved by recording the interference pattern between an object wave front and a coherent reference beam. The use of a silver halide emulsion as an energy-recording medium requires chemical processing in order to manifest the wave-front modulation. Wave-front reconstruction takes place, in a third step, when the hologram is illuminated with a second reference wave. Under certain conditions, the reconstructed wave front is identical in form to the original wave front, and may be manipulated as if it were the original beam.

Expressions describing the interference and modulation between the object wave and the reference wave show the means by which the amplitude and relative phase information are preserved. Let the object wave and reference wave be represented, respectively, by

$$\text{(Object)} \quad O(x,y)e^{i[-\omega_1 t + \alpha x + \gamma z + \psi(x,y)]}$$

$$\text{(Reference)} \quad R(x,y)e^{i[-\omega_2 t + \delta x + \mu z + \phi(x,y)]}$$

where $O(x,y)$, $\psi(x,y)$ and $R(x,y)$, $\phi(x,y)$ represent the amplitude and phase distribution pairs of the object and reference waves, respectively (see Fig. 18.5). The relationships between the incident angles, χ and θ, and the pairs of propagation constants, α, γ, and δ, μ of the object wave and reference wave, respectively, are the following:

$$\alpha = k \sin \chi, \; \gamma = k \cos \chi$$

$$\delta = k \sin \theta, \; \mu = k \cos \theta.$$

The temporal frequencies, ω_1 and ω_2, have units of radians/second. Square law detection of the interference signal between these two waves by the holographic plate produces a signal, $S(x,y)$, described by

$$S(x,y) \propto O^2(x,y) + O(x,y)R(x,y)\, e^{i[2\alpha x + \psi(x,y) - \phi(x,y)]} + R^2(x,y) + O(x,y)R(x,y)\, e^{-i[2\alpha x + \psi(x,y) - \phi(x,y)]}. \quad (1)$$

Wave-front reconstruction is achieved by propagating a second reference wave through the holographic plate. Let the new reference wave be represented by $W(x,y)$,

$$W(x,y) = R'(x,y)e^{i[-\omega t + \epsilon x + \Omega(x,y)]}$$

where ϵ is the propagation constant, $\epsilon = k \sin \beta$, and β is the incident angle of the reference beam. $R'(x,y)$ and $\Omega(x,y)$ represent the amplitude and phase distribution of the new reference beam. If the reconstructing wave propagates along the same path as the original reference wave then the object amplitude is given by

$$E_{obj} = R'(x,y)O(x,y)R(x,y)\, e^{i[-\omega t + \alpha x + \Psi(x,y) - \phi(x,y) + \Omega(x,y)]}. \quad (2)$$

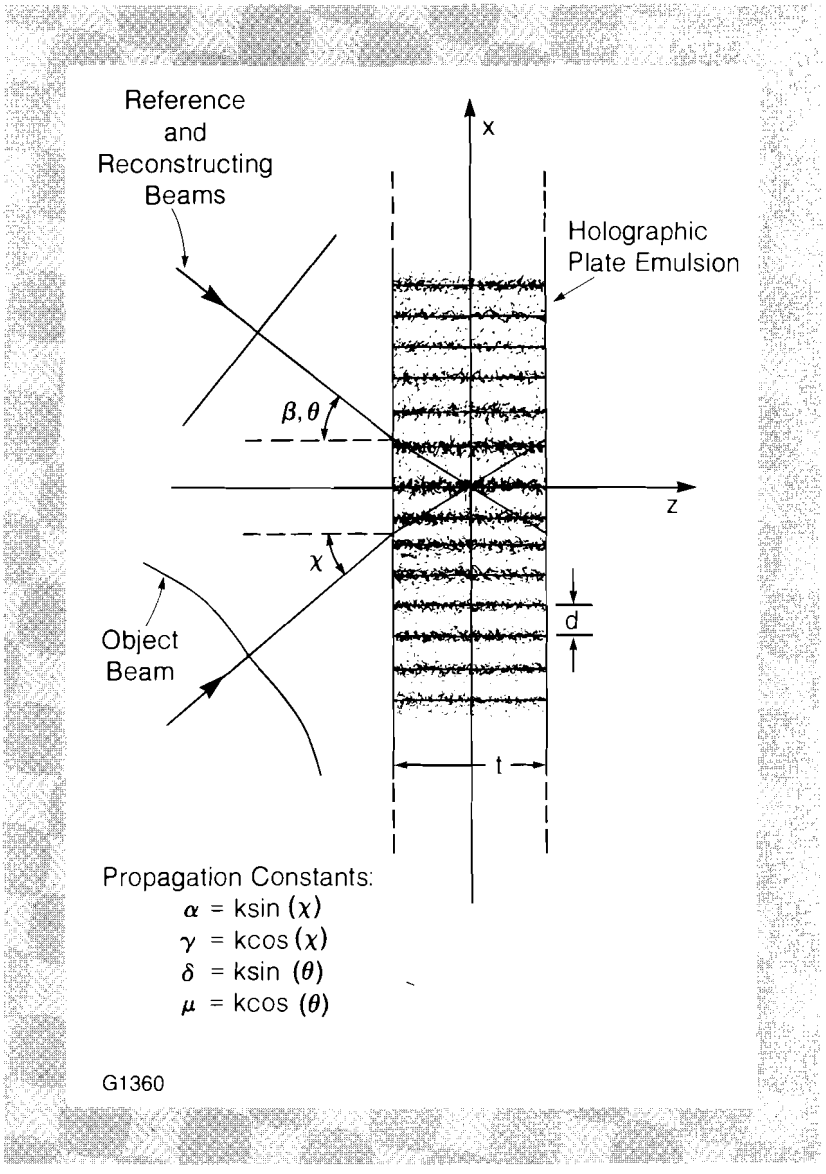

Fig. 18.5
The object and reference beams interfere symmetrically with respect to the normal to the holographic plate so that $\theta = -\chi$. The cw reconstructing-reference beam follows the same path as the pulsed-reference beam so that $\beta = \theta$.

The propagation constant, α = ksin χ, shows that the reconstructed object wave travels along the same path as the original object wave. Equation (2) shows that nominally plane-wave reference beams, containing slowly varying phase errors, are adequate as reference beams as long as the condition that $\Omega(x,y) - \phi(x,y)$ = constant is satisfied. Differences between the two phase distributions translate directly into the phase distribution of the reconstructed object wave. Equation (2) also shows that any amplitude nonuniformities, in either reference wave, translate directly into nonuniformities in the reconstructed-object amplitude. Therefore, linear recording of the object beam requires that the holographic system be able to select a portion of the original wave, and produce from it a uniform amplitude distribution to serve as the reference beam.

The filtering of the high-frequency Fourier components of a wave front results in increased amplitude uniformity. A system which is

capable of making the spatial-frequency spectrum physically accessible, for accurate filtering, is shown in Fig. 18.6. An entrance lens is placed at the center of a large obstruction, and used to expand a small portion of the original wave. The recollimation of this beam produces a plane-wave reference, which is a relatively simple phase distribution to reproduce. For a wave front with several wavelengths of aberration, a small portion of the wave front possesses a small fraction of a wavelength in phase variation, guaranteeing a nominally plane reference wave.

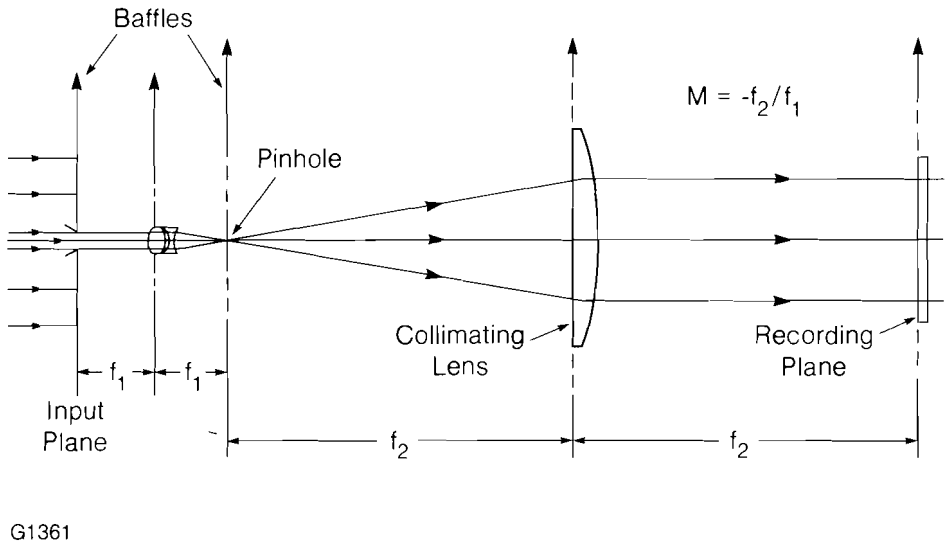

Fig. 18.6
The spatial filter system selects a 3.8-mm-diameter portion of the pulsed beam, filters out the high frequency content with a 15-μm pinhole, and produces a more uniform plane-wave reference beam at the holographic recording plane ($M = -f_2/f_1 = 22$).

The heart of the holographic experimental setup (Fig. 18.7) is a holographic interferometer. The use of a Galilean down-collimating telescope allowed a compromise between studying the GDL-pulsed wave front and using standard-format, 5″ by 4″, Agfa-Gevaert 10E56 holographic plates. The incident wave front was split into a reflected-object beam and a transmitted-reference beam. A central region of the transmitted beam continued through an input aperture, passed through focus to be filtered, and was recollimated. A magnification of ~ 22 produced an 83-mm-diameter reference beam which overfilled the 63-mm-diameter demagnified object beam. The two beams recombined at the holographic plate to form an interference pattern that was characteristic of both the object and the reference beam. A cw laser, operating at the same wavelength, was used with the same setup to reconstruct the object wave front.

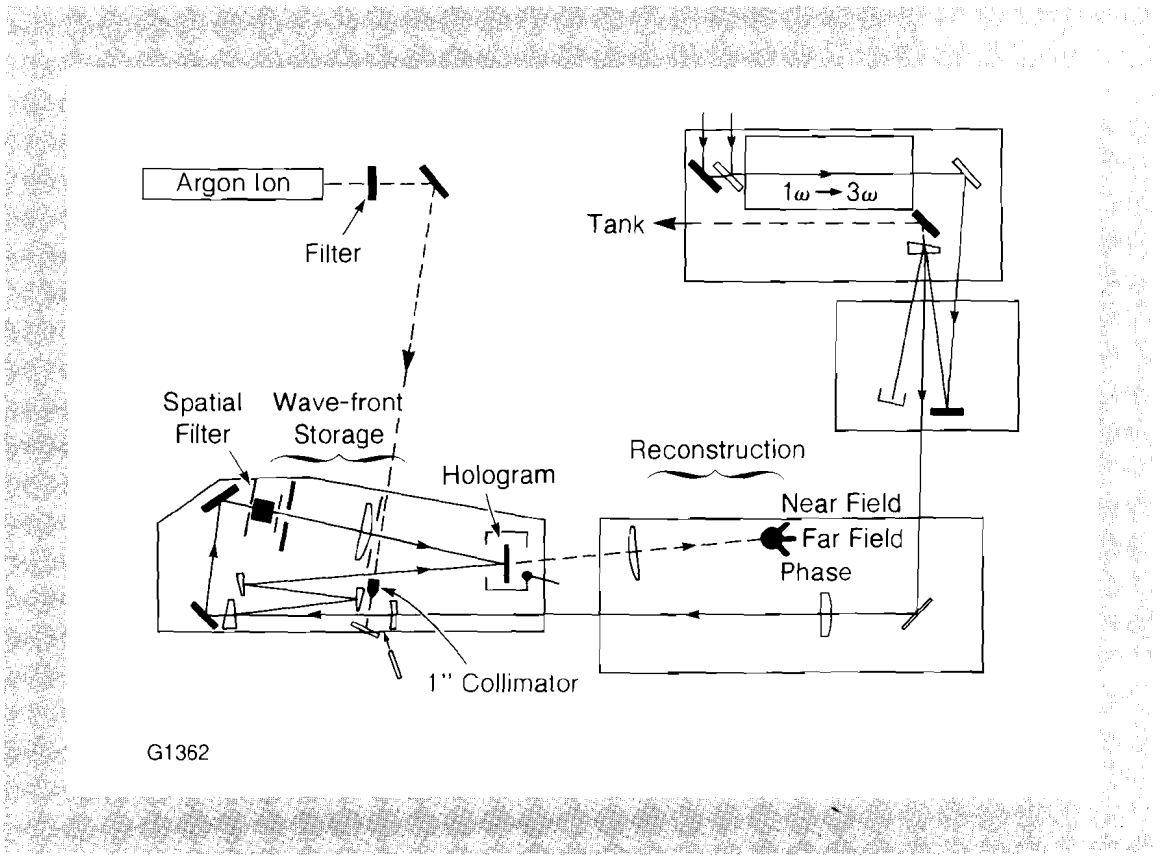

Fig. 18.7
The holographic experimental setup consists of two systems. First, the wave-front storage system includes beam-steering optics which direct the pulsed beam through the two arms of the holographic interferometer, where the reference beam path is delineated by the spatial filter and the object beam path contains three bare surface reflectors. The two paths cross at the holographic recording plane, where the interference pattern between the pulsed object and reference beam is stored in the form of a hologram. Secondly, the wave-front reconstruction system includes a cw argon ion laser which is injected into the reference beam path to produce a colinear reconstructing plane-wave reference beam. The reconstructed wave front that emanates from the hologram is measured by means of near-field and far-field cameras and several interferometers.

Holographically Reconstructed Wave-Front Measurement

Conventional wave-front-measurement techniques were applied to both the reconstructed beam and the pulsed beam in order to provide a means of evaluation for the holographic technique. The image-processing system at the LLE was used to digitize and intensity-correct the photographic data, and to perform computer-based manipulations and statistical calculations on these images. Reconstructed near-field (Figs. 18.8 and 18.9) and quasi-far-field (Figs. 18.10 and 18.11) intensity distributions closely resemble those obtained from conventional techniques. Reconstruction of the near-field intensity profile was achieved with an overall resolution approaching 2 lines/mm, and an azimuthally averaged, peak-to-valley intensity-modulation increase of about 50%. The resolution of the reconstructed quasi-far-field intensity profile was nearly the same, 1-2 lines/mm, but the peak-to-valley intensity-modulation increase was 90%. The resolution was limited by both halation effects and scattering at the holographic plate. The intensity-modulation increase is symptomatic of a nonlinearly recorded amplitude distribution, attributable to an excessive object-to-reference beam-intensity ratio and amplitude nonuniformities in the pulsed-reference beam.

Figure 18.12 shows both the pulsed and the reconstructed-object-beam lateral-shearing interferograms. A direct comparison can be made since the amount of shear is, within a few percent, the same. The time-dependent phase effects, clearly evident in the pulsed interferogram, are reduced in the reconstructed interferogram. The

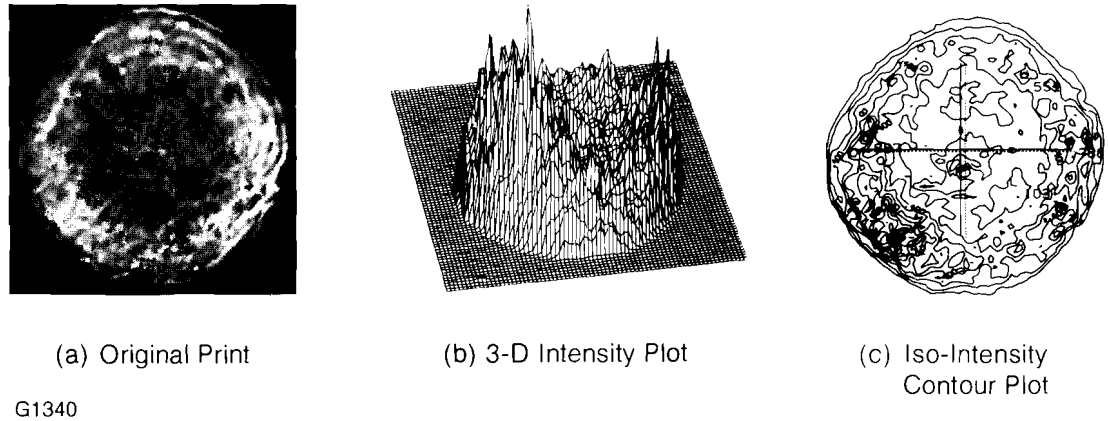

Fig. 18.8
A near-field photograph of the demagnified GDL frequency-tripled laser beam is used as a point of reference for evaluation of the holographically produced near-field distribution.

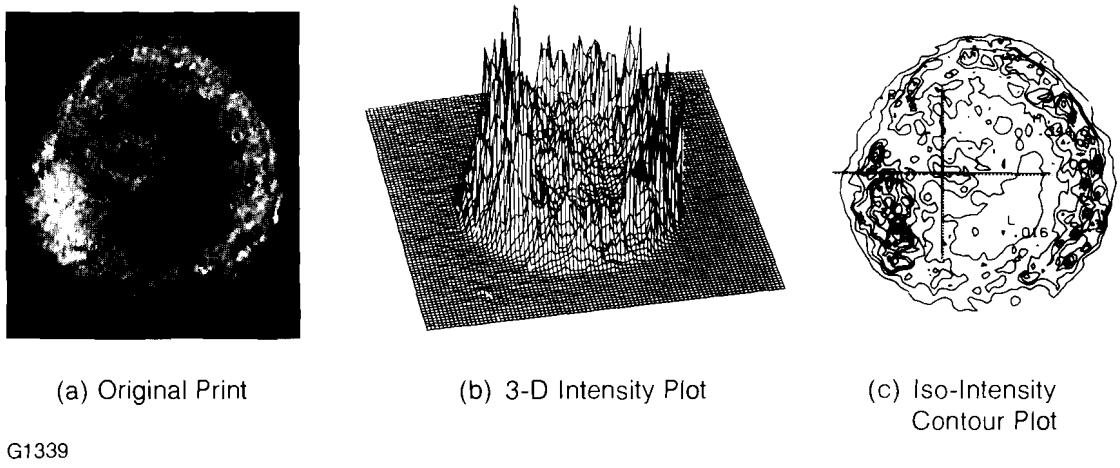

Fig. 18.9
The reconstructed near-field intensity distribution closely resembles the pulsed near-field profile, but a modulation increase due to non-linear recording is evident.

number of fringes, as well as their orientation, is the same in each pattern. Small, rapidly varying changes in the shape of each fringe, of the same magnitude observed between measurements of different laser pulses, are present. Additionally, small, slowly varying differences in the shape of the fringes corresponding to optical-path differences of about one-half to one wavelength of light, are readily attributable to OPD variations in the holographic plate.

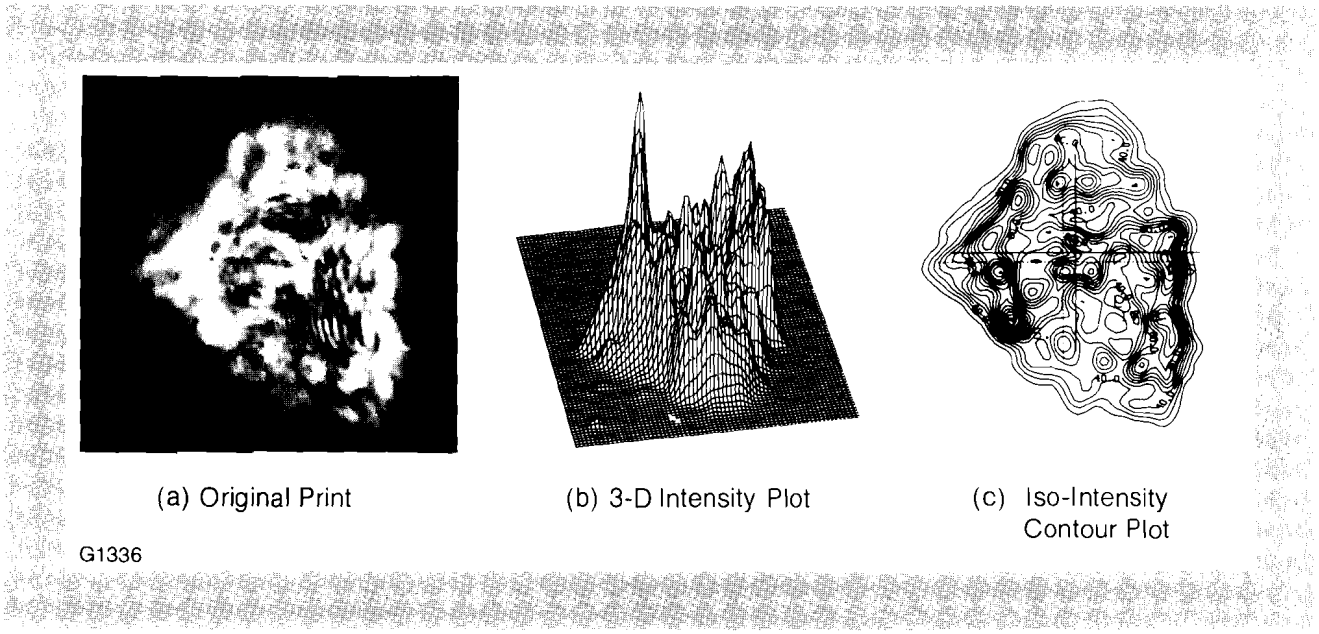

Fig. 18.10
A far-field photograph of the GDL frequency-tripled laser beam is used as a point of reference for evaluation of the holographically produced far-field distribution.

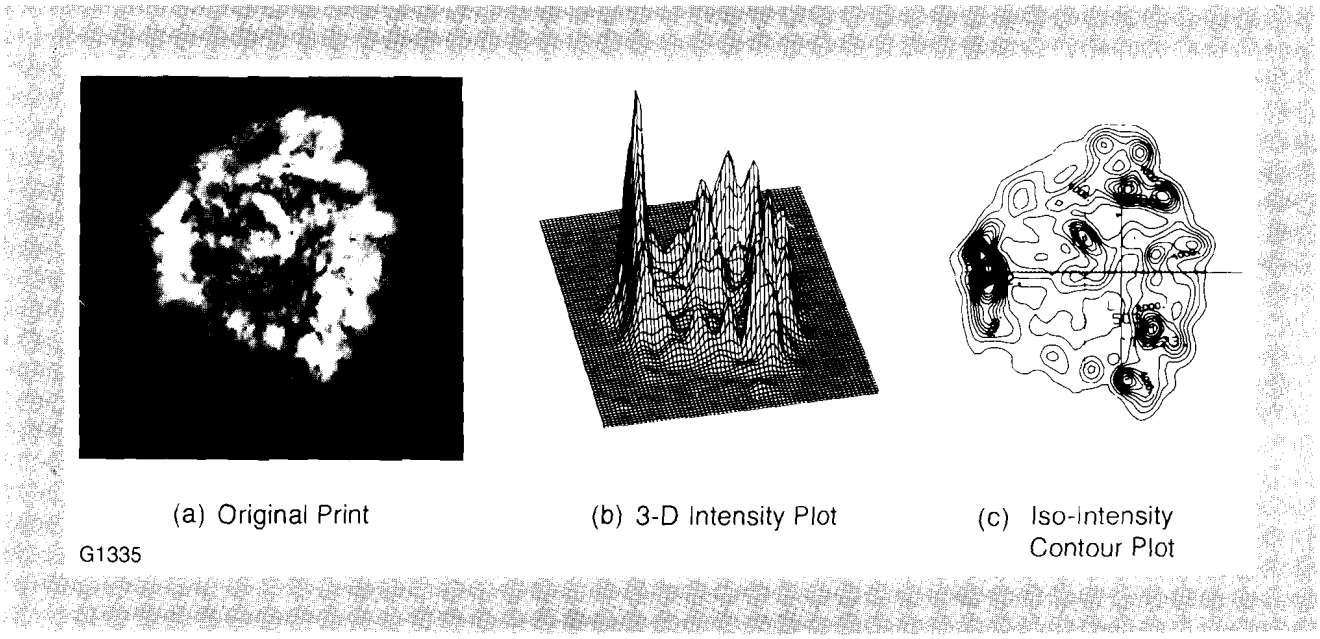

Fig. 18.11
The reconstructed ETP array closely resembles the pulsed ETP results, but nonlinear recording and OPD errors presently limit the accuracy of far-field imaging.

The final experiment at $\lambda = 351$ nm, conducted on the reconstructed object wave front, produced a 2-D measurement of the phase front. A bleached hologram was placed at the original recording plane. A point-diffraction interferometer (Smartt PDI) was positioned at the focus of an F/3 lens, and a UV vidicon camera was placed

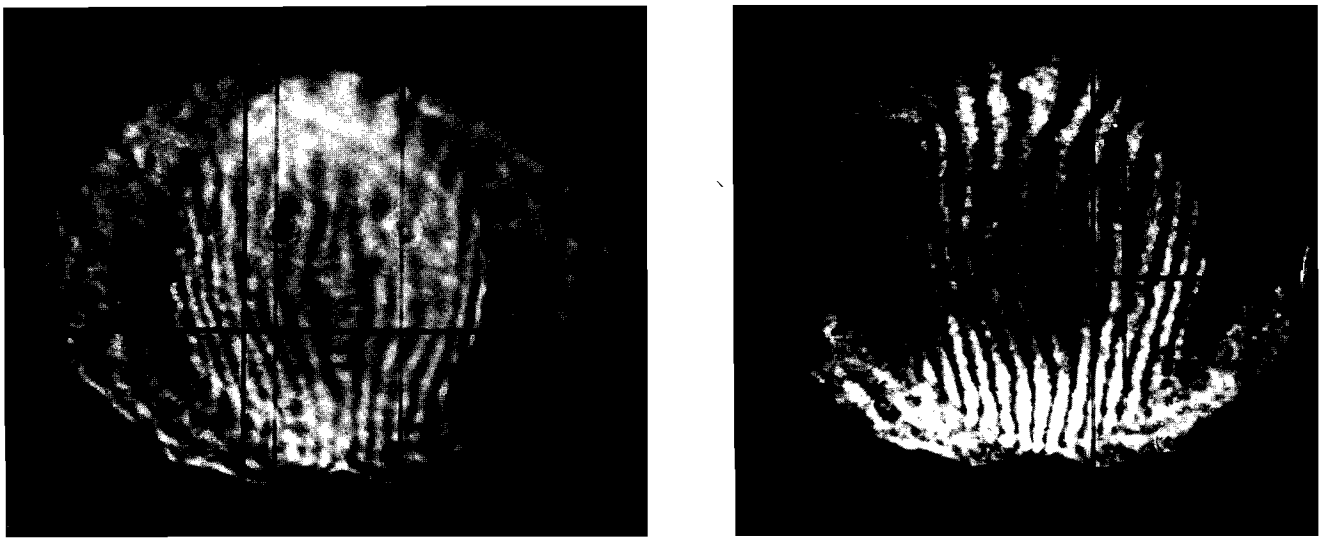

pulsed reconstructed

G1337

Fig. 18.12
Lateral-shearing interferograms provide information about the derivative of the phase front. Pulsed and reconstructed interferograms have the same number of fringes and the same orientation, indicating an accurate phase-front reconstruction.

immediately behind the PDI to aid in the alignment of the interferometer. An interferogram obtained with the point-diffraction interferometer is shown in Fig. 18.13(a). It represents the cumulative phase distortion due to the object beam, the holographic plate, the focusing lens, and the defocus introduced by the axial position of the PDI pinhole. Large variations in the fringe visibility, inherent in the application of the PDI to highly aberrated phase fronts, are observed. An additional experiment was performed to determine the requirements for conventional holographic interferometry. A holographic interferometer was constructed on a pneumatically stabilized optical table. The reconstructing and reference beams were derived from a Helium-Neon laser. The reconstructed wave front was combined with the directly transmitting wave front from the other arm of the system to form two-beam interference fringes as shown in Fig. 18.13(b). The OPD variations of the holographic plate were removed from the interference pattern by passing the reference beam through the plate, coincident with the reconstructed beam. Eight to nine defocus fringes are counted from center to edge. These correspond to 8.5 wavelengths of defocus at $\lambda = 632.8$ nm, or about 15 wavelengths at $\lambda = 351.1$ nm. The seven to eight fringes over half of the field of the shearing interferograms also correspond to $\sim$ 15 wavelengths of defocus at $\lambda = 351.1$ nm. With defocus as the measure of comparison, the shearing interferometry is in close agreement with the holographic interferometry.

Summary

Holographic techniques have been successfully implemented on a UV, frequency-tripled, high-peak-power laser in order to obtain cw reconstructions for conventional wave-front measurements. Near-field amplitude and phase distributions from the GDL frequency-converted laser have been holographically recorded on silver-halide emulsions. Previously the absence of a suitable reference beam forced one to use some type of shearing interferometry to obtain phase-front information, while the near-field and far-field distributions

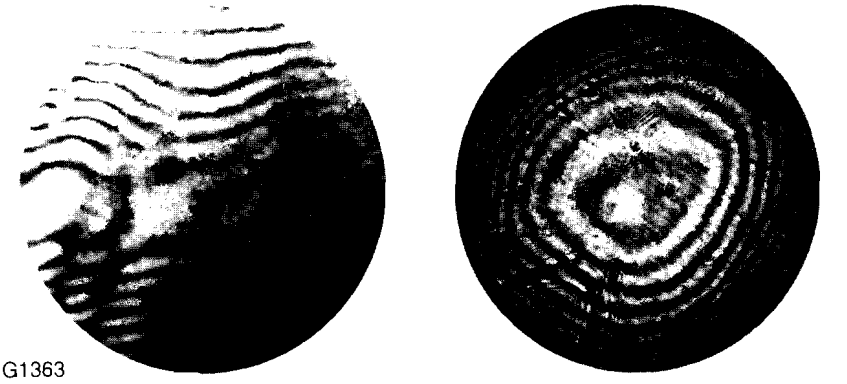

(a) Point-Diffraction Interferometer

(b) Holographic Interferometer

Fig. 18.13
The point-diffraction interferometer (a) yields 2-D phase-front information by means of a locally generated reference beam derived from the aberrated point-spread function of the test wave front. The holographic interferometer (b) yields 2-D phase-front information by means of a separate plane-wave reference beam. The difference between these results is primarily a defocus term in the point-diffraction interferogram (a).

were recorded as intensity profiles. A spatially filtered, locally generated reference beam was created to holographically store the complex amplitude distribution of the pulsed laser beam, while reconstruction of the original wave front was achieved with a cw laser.

Although the reconstructed intensity profiles closely resemble those obtained from conventional methods, we conclude that this technique does not presently reproduce the laser amplitude distribution with sufficient accuracy to replace conventional intensity measurement techniques. However, it is believed that several improvements can be made, especially with regard to system flexibility, that would greatly reduce the sources of noise and the sources of nonlinear amplitude recording. Furthermore, this technique presently provides the means to study the relationship between phase correction (wave-front modulation) and the corresponding changes in the intensity distribution at the real target plane.

Accurate phase-front reconstruction was demonstrated, with the optical path variations of the holographic plate limiting the measurement accuracy to one-half wave (λ = 351 nm) for the central 75% of the beam's area, and to one wave for the edge of the beam. Additionally, several two-beam interferometric techniques, not practicable with a high-peak-power laser, have been successfully implemented on a cw reconstruction of the pulsed laser beam.

ACKNOWLEDGMENT

This work was supported by the U.S. Department of Energy Office of Inertial Fusion under contract number DE-AC08-80DP40124 and by the Laser Fusion Feasibility Project at the Laboratory for Laser Energetics which has the following sponsors: Empire State Electric Energy Research Corporation, General Electric Company, New York State Energy Research and Development Authority, Northeast Utilities Service Company, Southern California Edison Company, The Standard Oil Company, and University of Rochester. Such support does not imply endorsement of the content by any of the above parties.

REFERENCES

1. LLE Review **12**, 5 (1982).

2. LLE Review **7**, 5 (1981).

2.C Hydrodynamic Simulations of Thermal Self-Focusing in Laser-Generated Plasmas

Self-focusing of the incident laser radiation in the underdense coronal plasmas of laser-fusion targets has long been recognized as a mechanism which can enhance irradiation nonuniformities, thus disrupting the high-compression implosions of these targets. This phenomenon is understood to involve a close interaction between perturbations to the plasma density profile caused by thermal or ponderomotive pressure gradients and propagation of the laser in the perturbed plasma. Numerous experimental observations of self-focusing in underdense plasmas have been reported.[1] As laser-fusion research moves towards larger targets, producing longer density scale lengths in the underdense corona, the possibility of thermal self-focusing will become an increasingly serious consideration. For this reason, we have performed a number of simulations of this mechanism, including realistic 2-D hydrodynamics.

A distinction is generally made between thermal and ponderomotive self-focusing. In the first case, the thermal pressure associated with a laser-heated plasma causes a reduction in the plasma density and, therefore, an increase in the plasma refractive index; in the geometrical-optics approximation, incident laser rays are then refracted in such a way as to enhance the perturbation. In ponderomotive self-focusing, sometimes referred to as filamentation, it is the ponderomotive force of an intense electromagnetic wave that distorts the plasma. This latter mechanism is expected to be particularly effective for perturbations with short spatial scale lengths, typically as small as the wavelength of the incident radiation, provided that the laser intensity is sufficiently high so that the ponderomotive pressure can balance the pressure jump associated with a significant electron-density perturbation. Thermal self-focusing is expected to be less important on these scale lengths, as it is difficult to sustain a thermal pressure gradient over distances which are, in typical cases, comparable to or less than an electron mean free path. On the other hand, for larger-scale-length modulations, thermal conduction is less effective in smoothing out temperature perturbations, and we expect thermal self-focusing to be the dominant mechanism. There may be situations where self-focusing is initiated by the thermal mechanism, but subsequently develops into ponderomotive self-focusing after the beam is focused to a small diameter. Here, however, we will confine our discussion to thermal self-focusing.

Many theoretical treatments of thermal self-focusing have been reported in the literature.[2,3] Generally, simplifying assumptions are made about the plasma behavior, although full 1-D hydrodynamic calculations have been performed.[3] In actual experimental situations, the electron-density distribution and, hence, the refractive index in the plasma corona are dependent on the full time history of the hydrodynamics; and the interaction process thereby becomes considerably more complex than can be treated analytically. The electromagnetic energy propagation must be coupled self-consistently with the 2-D

plasma hydrodynamics, including the heating and ablation processes. The purpose of this article is to present a number of such calculations, covering a broad range of conditions, using the 2-D Eulerian hydrodynamics code *SAGE* which includes a self-consistent ray-tracing algorithm for energy propagation and absorption. These calculations are not limited in relevance by the use of simplified hydrodynamic models, and are therefore able to follow the full temporal evolution of the self-focusing process. In general it is whole-beam self-focusing which is modeled here, but, to the extent permitted by the resolution of the computational grid and the neglect of diffraction, small-scale self-focusing is also modeled. The price paid for a more realistic hydrodynamic treatment is a less realistic electromagnetic propagation model, since the geometrical-optics assumption implied by the use of ray tracing excludes diffractive effects; however, this is probably not a serious concern for a wide range of experiments carried out in the near field of a laser beam, particularly for the conditions of interest in this article.

On account of the wide range of initial conditions and plasma configurations that may be encountered, we will not attempt to seek specific criteria which will determine simply, in a binary sense, whether or not self-focusing occurs. It is more instructive to consider a variety of cases which illustrate the circumstances in which self-focusing is likely to develop, and demonstrate the nonlinear evolution of the process. Variables such as the laser wavelength, pulse width and spatial intensity profile, and the initial plasma density and temperature profiles, can all be important. It is possible, however, to draw some general conclusions; for example, whole-beam self-focusing is more likely to occur when the beam diameter is small (typically less than the plasma scale length), when the background plasma is cold, and when the incident laser intensity is high.

Computational Model

For the calculations reported here, the code *SAGE* has been used in 2-D cylindrical geometry (r,z). The simplest physical model needed to treat realistically the dynamics of the underdense plasma has been adopted. A perfect-gas equation of state and a one-temperature fluid are assumed; and radiation emission, suprathermal-electron generation, and magnetic-field effects are omitted. Thermal conduction is modeled using a standard "flux-limiter" formulation,[4] in which the heat flux $\mathbf{q}$ is directed antiparallel to the temperature gradient but limited in magnitude to a given fraction of the free-streaming flux. For the low-atomic-number (CH) targets considered here, most of these assumptions are well justified. Calculations with *SAGE*, including a more complete physical description, show that (1) a real equation of state is unnecessary since the corona is fully ionized; (2) use of a two-temperature model leads to results similar to those obtained from the one-temperature model since the ions have a low heat capacity compared with the electrons; and (3) radiation emission is small. Suprathermal electrons generated at the critical density by resonance absorption are unlikely to be important for the short wavelengths and long scale lengths under consideration. On the other hand, magnetic fields could be important, particularly if steep temperature gradients

resulting from self-focusing enhance their generation, but their treatment is outside the scope of this paper. The flux-limited treatment of thermal conduction, although ad hoc, is required to provide a reasonably accurate calculation of the absorption fraction.[5]

The code *SAGE* makes use of a general, fully three-dimensional (3-D), ray-tracing model (TRACER-3) which calculates ray trajectories through arbitrary refractive-index profiles.[6] A ray trajectory, parametrized by the path distance s, is given by $\mathbf{r}(s)$ where $\mathbf{r}$ obeys the equation[7]

$$\frac{d}{ds}\mu\frac{d\mathbf{r}}{ds} = \nabla\mu \tag{1}$$

with μ the refractive index. For a plasma, $\mu = (1-n_e/n_c)^{1/2}$, where n_e is the local electron density and n_c is the critical electron density corresponding to the wavelength λ of the irradiation. Equation (1) is integrated by introducing the direction-cosine vector, $\mathbf{c}$, and solving the coupled first-order equations

$$\frac{d}{ds}\mathbf{r} = \mathbf{c} \tag{2}$$

$$\frac{d}{ds}(\mu\mathbf{c}) = \nabla\mu\ . \tag{3}$$

The absorption fraction is calculated from the integral of the inverse-bremsstrahlung coefficient K_{IB} along the ray path. The refractive index $\mu(s)$ is determined here by interpolation from the electron-density distribution n_e stored on the 2-D hydrodynamic grid. The limiting factor affecting the accuracy of the trajectory calculations reported here is the resolution of the grid, which limits the accuracy with which $n_e(\mathbf{r})$ and therefore $\mu(\mathbf{r})$ are known. In all of these simulations, at least 50 rays are followed each timestep for typically 1000 hydrodynamic timesteps. Almost identical results are obtained in cases where only half as many rays are used each timestep. For a given amount of computer time, better statistics are probably obtained using 50 rays each timestep rather than ~ 500 rays every ten timesteps, since small noise perturbations in ray directions are induced by small noise fluctuations in the (changing) electron-density profile.

In summary, the four main physical processes being modeled are basic hydrodynamics, thermal conduction, inverse-bremsstrahlung absorption, and refraction. All of these play important roles in determining the onset and development of thermal self-focusing in laser-produced plasmas.

Illustrative Calculation

We will commence by examining a "standard" calculation, which clearly exhibits whole-beam self-focusing, before proceeding to consider some parametric variations. The laser is assumed to have a wavelength of 351 nm, Gaussian temporal and spatial profiles, a pulse length (full width at half maximum) of t_{FW} = 600 ps, and a nominal beam radius r_{90} (defined at the 10% intensity point or equivalently the

90% energy point) of 200 μm. The peak intensity in space and time is 9×10^{14} W/cm^2, and the nominal intensity I [defined as $J/(\pi r_{90}^2\ t_{FW})$ where J is the laser energy] is 4×10^{14} W/cm^2. The spatial profile is actually truncated at the nominal radius, the intensity being set to zero for $r > r_{90}$; this is done to avoid tracing many rays which carry little energy.

The plasma is assumed to have an initial exponential density profile of (e-folding) scale length L = 500 μm, and it is assumed to be cold (we use an initial temperature of 0.01 eV). This configuration corresponds quite closely with experiments in which a high-intensity beam interacts with a long-scale-length preformed plasma; for example, an experiment using a 1-μm wavelength but otherwise similar parameters was recently reported[8,9] and provided some indications of self-focusing.[9] This configuration (but with a higher background temperature) could also relate to situations where a hot spot appears in a laser beam some time into the interaction, after the plasma has developed a large scale length. One important dimensionless parameter, R, which may be thought of as the relative beam radius, is defined as the ratio of the beam radius to the plasma scale length: $R = r_{90}/L$. For the standard case, R = 0.4. It will become apparent that R and the other parameters have been chosen to facilitate whole-beam self-focusing.

Results are presented in Fig. 18.14, at four successive times measured relative to the peak of the pulse. Electron-density contours are drawn at the critical density n_c and at integer powers of $2 \times n_c$. The laser is incident from the right, along the target normal, with rays propagating initially parallel to the z axis. Rays are followed in the hydrodynamic calculation until all but one part in 10^5 of their energy is deposited or until they leave the simulation region. In the plotting program, however, they are terminated when 90% of their energy has been deposited. Here, and in most of the other calculations, the initial radii of the rays are distributed uniformly over $0 \leq r \leq r_{90}$, 50 rays are used per calculation cycle, and one out of every three rays is plotted. This calculation employed 60 grid points uniformly spaced in the z direction, and 24 in the r direction, variably spaced with the smallest zones near the z axis and the zone size expanding by a constant ratio from zone to zone.

Whole-beam self-focusing is observed to have occurred by the peak of the pulse [Fig. 18.14(c)]; its origin may be traced from the earlier plots [Figs. 18.14(a) and 18.14(b)]. Early in time [Fig. 18.14(a)], the laser is absorbed efficiently by the initially cold underdense plasma below quarter-critical. On the axis, where the incident intensity is the highest, the plasma is heated the most; the inverse-bremsstrahlung absorption coefficient K_{IB}, which scales as $T_e^{-3/2}$, is therefore reduced more on-axis than off-axis, resulting in the enhanced propagation of the 90%-energy-deposition contour on-axis as seen in Fig. 18.14(a). Material is ablated from the heated region, back toward the laser and also radially outward. The radial pressure gradient is initially strong at the edge of the beam, at the discontinuity resulting from truncating the radially Gaussian intensity profile at the

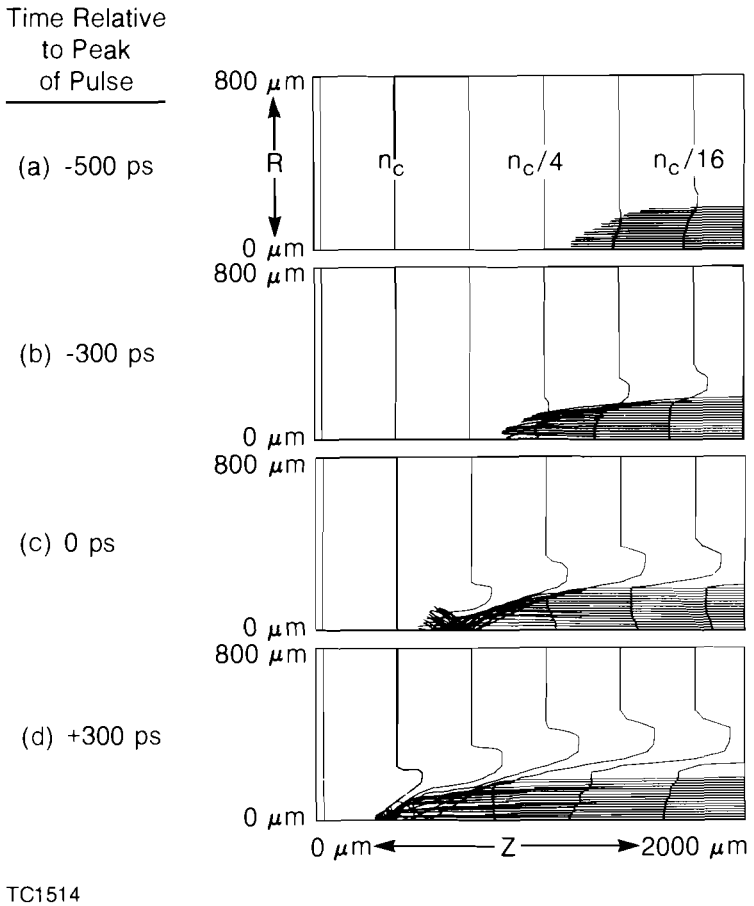

Fig. 18.14
Results at four times during the standard calculation. Time is measured relative to the peaks of the laser pulse and the laser pulse is propagating from right to left. The electron density contours are shown for the critical density n_c and at integer powers of $2 \times n_c$. The rays are terminated when 90% of their energy has been absorbed. Whole-beam self-focusing is clearly evident at the peak of the laser pulse (c).

10% intensity point. Incident rays are then refracted into this low-density region, their deflections becoming greater as they approach the critical-density surface. It will be noted that some rays pass through the axis before terminating. Removal of mass from the central (on-axis) region is enhanced by both lateral expansion in the cylindrical plasma, and by the incident energy flux becoming more intense when focused onto the axis. Self-focusing is enhanced by both of these geometrical factors.

Parametric Variations

A comparison calculation is illustrated in Fig. 18.15. Here all the parameters are unaltered, except that the beam radius has been doubled and the laser energy increased by a factor of 4 to maintain the same intensity. The four plots correspond to the same times as in Fig. 18.14. In this case no significant self-focusing occurs: no rays are bent a significant fraction of the beam radius, with the exception of a few rays at the edge of the beam in Fig. 18.15(d). Here the plasma scale length is too small in comparison with the beam radius; quantitatively, the geometrical aspect ratio (or relative beam radius)

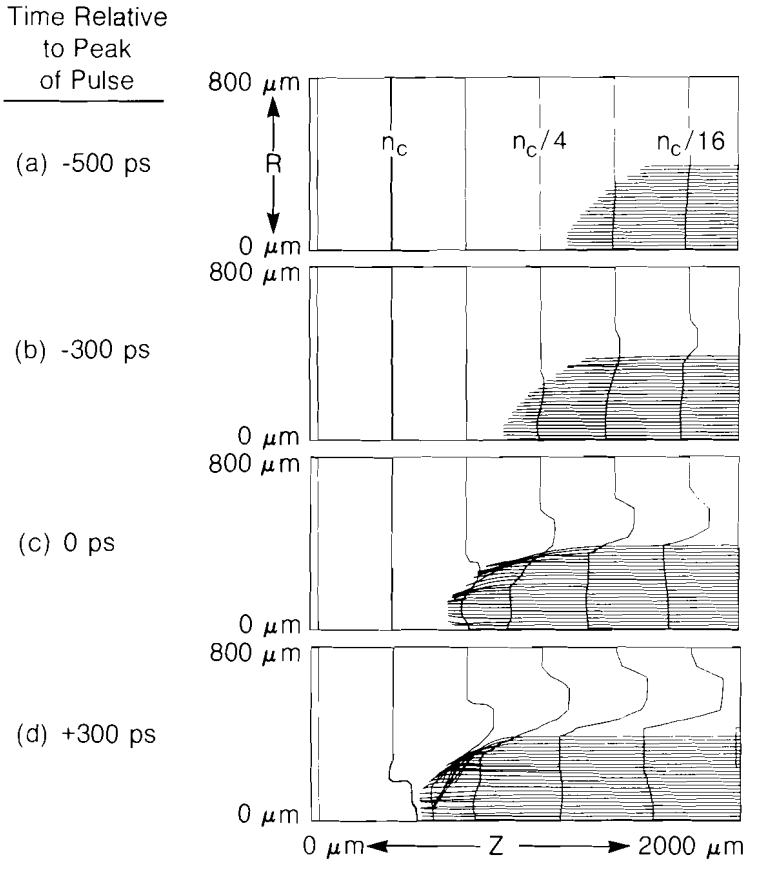

Fig. 18.15
Results for the standard parameters, but with the beam radius doubled while maintaining the intensity. Whole-beam self-focusing is not evident at the peak of the pulse.

r_{90}/L is 0.8, compared with 0.4 in the previous (standard) case. For the irradiation parameters under consideration, a threshold for significant self-focusing occurs at a value of r_{90}/L somewhere between these two values.

It is also interesting to compare the rates of propagation of the beam into the plasma in the two cases, measured along the z axis. Initially the burn front moves at the same speed (up to 300 ps before the peak of the pulse), but when self-focusing occurs in Fig. 18.14, the front penetrates faster and deeper into the plasma.

The effect of increasing the laser intensity may be readily seen by comparing Fig. 18.16, where the intensity has been doubled, with the standard case (Fig. 18.14). The same qualitative behavior occurs, the main difference being that the beam now propagates somewhat faster and self-focusing occurs somewhat earlier. At 300 ps before the peak of the pulse, a tight beam focus appears at half-critical, but this disappears by the peak of the pulse as a result of further expulsion of plasma from the underdense heated region.

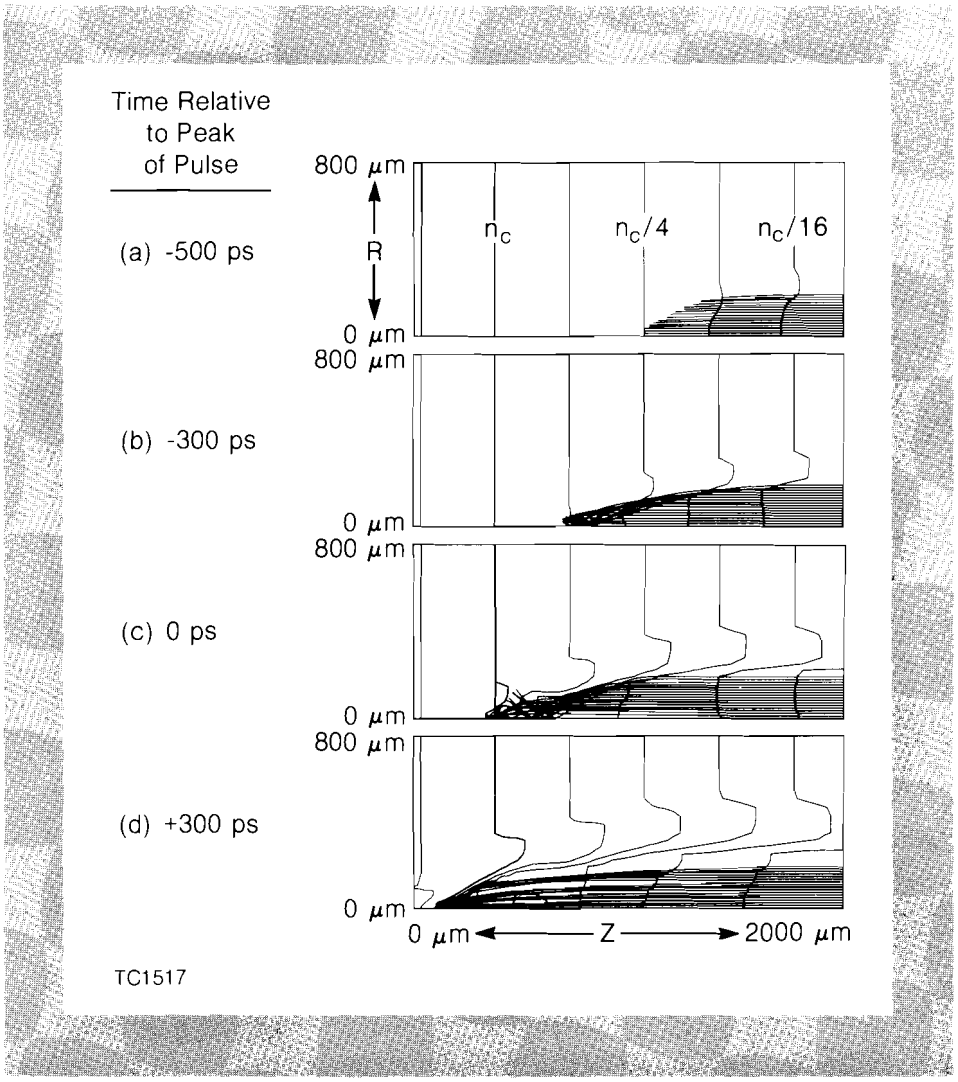

Fig. 18.16
Results for the standard parameters, but with the intensity doubled. Whole-beam self-focusing is evident as early as (b) and the propagation depth is increased due to the self-focusing.

To examine the effect of laser wavelength, the standard calculation has been repeated but with the laser wavelength increased by a factor of 3 to 1054 nm. Self-focusing also occurs in this case, as is shown in Fig. 18.17. The same initial density profile is used; thus, the critical surface appears further to the right. The laser quickly burns through the underdense plasma, reaching critical density by t = −500 ps [Fig. 18.17(a)]. Thereafter, whole-beam self-focusing results in a narrow conical-shaped burn front propagating into what was initially an overdense plasma. The increased complexity in Figs. 18.17(b) and 18.17(c) arises because of the reduced inverse-bremsstrahlung absorption that occurs at longer wavelengths: most rays have not suffered 90% attenuation by the time they reach the vicinity of the critical surface, and so their return trajectories are plotted.

It is interesting to note that these rays return well-collimated toward the incident laser, even though they undergo substantial angular spreading in the vicinity of critical. In this calculation approximately half of the incident laser energy is reflected, and 80% of the reflected light returns to within 12° of the laser axis (see Fig. 18.18). In the 3-D

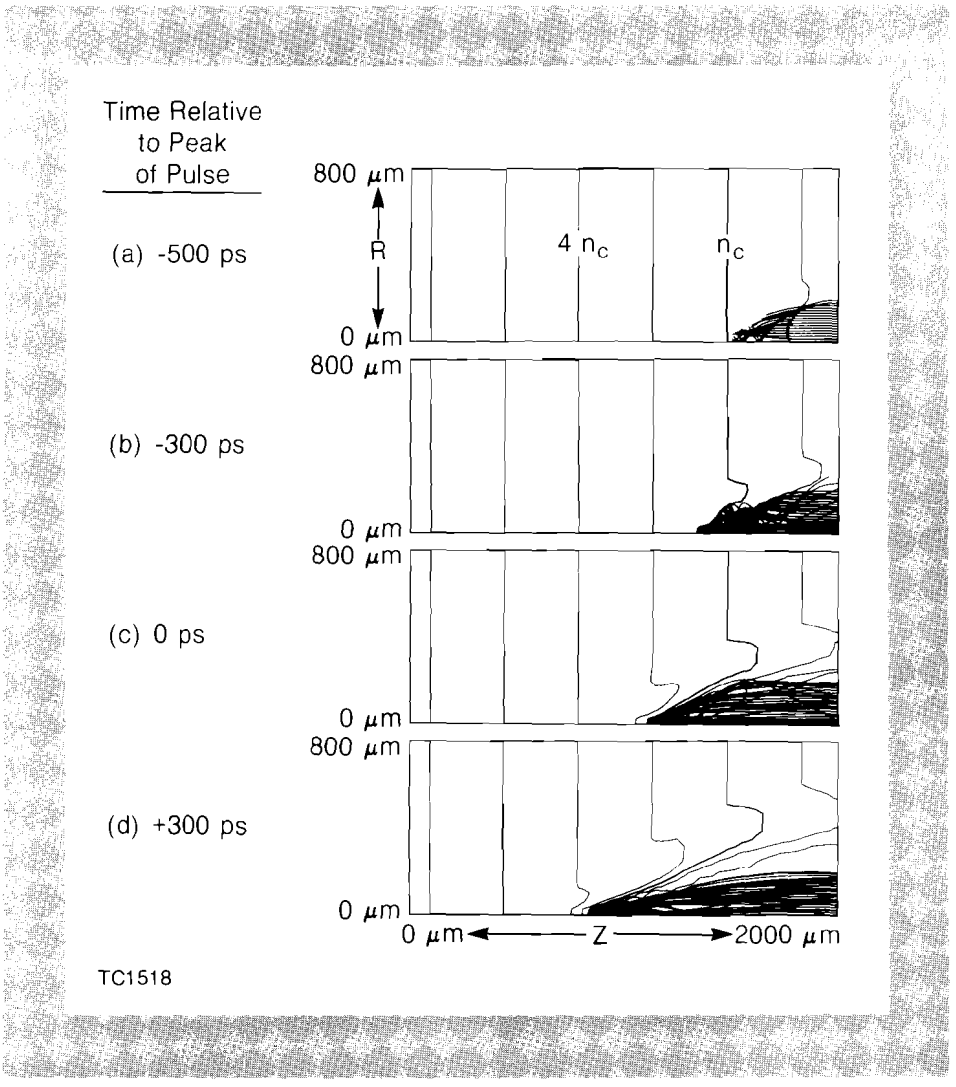

Fig. 18.17
Results for the standard parameters, but with the laser wavelength changed to 1054 nm. The same electron density profile is assumed, so the critical density is further to the right. A significant fraction of the rays reach the critical density before depositing 90% of their energy, so the reflected rays are also shown. Whole-beam self-focusing is present in (b).

configuration where the laser is obliquely incident on such a preformed plasma, it is reasonable to anticipate that the reflected light would also be directed toward the laser, rather than in the specular direction to the target normal, since the low-density channel is formed by the radial expulsion of plasma from the underdense laser-heated region. The inclusion of the ponderomotive force would probably enhance this effect. (At large angles of incidence, however, the ray trajectories may not be sufficiently bent in the vicinity of the turning point to return along the low-density channel.)

One factor which enhanced the self-focusing in the standard case was the cold background through which the beam propagated, since this plasma was easy to push aside radially. Distinctly different behavior occurs for a hot background, as is shown in Fig. 18.19, where the initial plasma temperature is taken to be 2 keV, comparable to the peak coronal temperature at the peak of the pulse in the standard case. Comparing Fig. 18.19 with Fig. 18.14, it is seen that substantially less lateral motion occurs in Fig. 18.19 because the background plasma is hot. Indented density contours still develop,

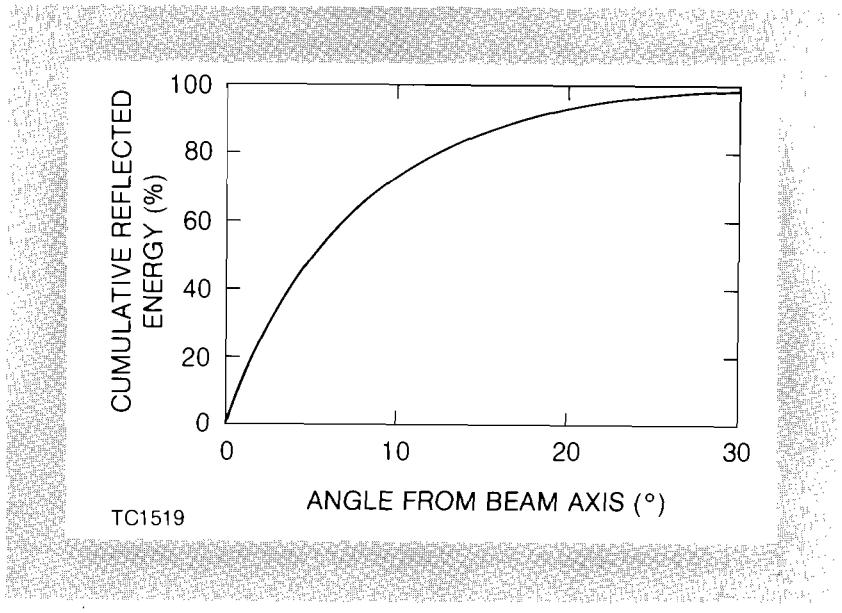

Fig. 18.18
Cumulative distribution of back-reflected light for the calculation of Fig. 18.17 which uses 1054-nm light. Note the strong collimation of the back-reflected light: 80% of this light returns within 12° of the laser beam axis.

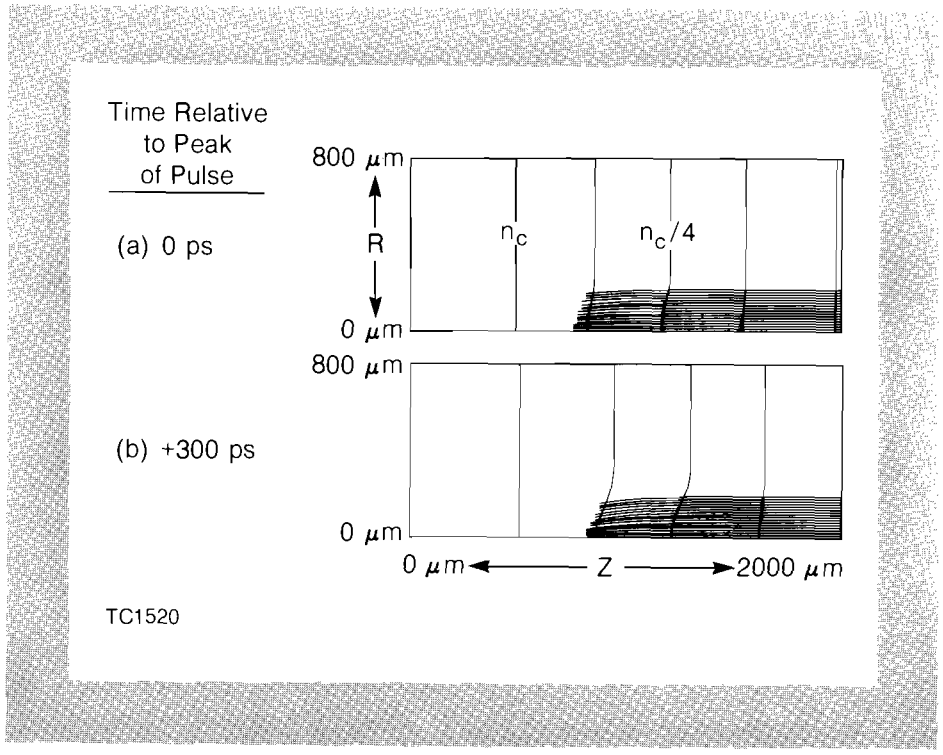

Fig. 18.19
Results for the standard parameters, but with the background plasma initially at the temperature of 2 keV. Only two times are shown because of the lack of whole-beam self-focusing.

but primarily as a result of greater ablation from the on-axis region which experiences the maximum incident-laser intensity. Self-focusing does not occur, and the depth of penetration of the beam front is considerably reduced relative to the standard case. In the intermediate case of a moderately hot background (1 keV), self-focusing similar to that observed in Fig. 18.14 is seen to occur.

The description of thermal energy transport is probably the biggest uncertainty in the processes modeled in this paper, so the sensitivity

of the results to the flux limiter f has been investigated. This parameter affects the heat flow both parallel and perpendicular to the laser axis. Results obtained using $f = 0.65$ indicate (reassuringly) that the basic self-focusing behavior observed in Fig. 18.14 is not significantly altered.

For laser-fusion applications, an important consideration is the effect of nonuniformity in the incident irradiation. Specifically, if a laser beam contains perturbations (hot spots), will small-scale self-focusing occur, seeded by these perturbations? To examine this question we have performed simulations in which the irradiation profile comprises a radial Gaussian superimposed upon a uniform background. The peak-to-background intensity ratio is varied, but the peak intensity is fixed at the same value as for the standard calculation. It is clearly not feasible, using a code with fewer than three dimensions, to simulate a beam containing more than one hot spot, since each hot spot would probably focus onto its own axis. If we were to impose an off-axis perturbation in our cylindrically symmetric geometry we could model the self-focusing of a ring perturbation, but experimentally it is more probable that such a ring filament would break up into a number of cylindrical filaments.

Results from a series of cases with successively smaller peak-to-background variations are shown in Fig. 18.20, all plotted at the peak of the pulse. In Fig. 18.20(a), the peak-to-background ratio is large (1.5:1), and in comparison with Fig. 18.20(c) it is seen that the hot spot self-focuses much as if the background had not been present. In Figs. 18.20(b)–18.20(d), the extent of self-focusing successively decreases, as expected, with a transition occurring somewhere between a 10% modulation and a 1% modulation. For real experimental situations, this transition point will of course depend on the detailed parameters: for example, a lower transition point would be expected for larger-scale-length plasmas. It is worth noting, though, that irradiation uniformities of better than a few percent should be attainable on multi-beam spherical systems.[10]

Conclusions

We have investigated thermal self-focusing in laser-produced plasmas, taking into account effects associated with realistic 2-D plasma hydrodynamics. While it is difficult, if not impossible, to draw quantitative conclusions about thermal self-focusing which will apply to all laser-plasma configurations, it is possible to note some general results. Whole-beam self-focusing has been observed, but only in situations where the beam radius is less than approximately half the plasma scale length. On-axis low-density channels in the underdense plasma have been seen to develop, primarily as a result of radial expansion from a heated region of finite radius, but also from preferential axial expansion from irradiation maxima. Light returning from such channels is expected to be well collimated toward the incident laser.

Experiments involving the interaction of a tightly focused laser beam with a cold, large-scale-length, preformed plasma are expected

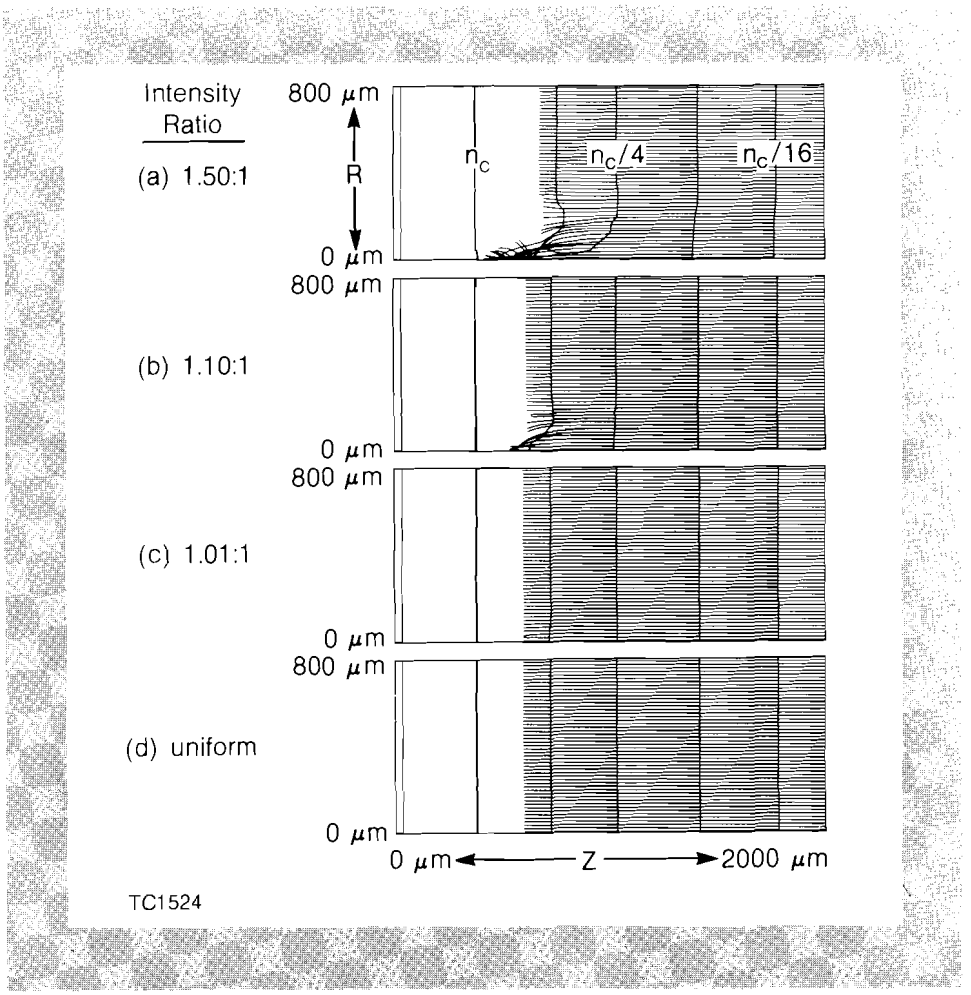

Fig. 18.20
Results for the standard parameters, but with the Gaussian beam superimposed on a uniform background to simulate a hot spot in the incident laser beams. The peak intensity in the Gaussian is held constant at the standard value and the background intensity is changed to generate the intensity ratios noted in the figure. All plots are at the peak of the laser pulse. The transition to whole-beam self-focusing occurs between a 1% and 10% intensity ratio.

to be particularly subject to thermal self-focusing. On the other hand, strong self-focusing is less likely to occur in situations where the background is warm and the laser radiation is uniform with small modulations. It is to be hoped that this latter state of affairs will apply to laser-fusion experiments as longer-scale-length plasmas are encountered. These results are discussed in greater detail in Ref. 11.

ACKNOWLEDGMENT

This work was supported by the U.S. Department of Energy Office of Inertial Fusion under contract number DE-AC08-80DP40124 and by the Laser Fusion Feasibility Project at the Laboratory for Laser Energetics which has the following sponsors: Empire State Electric Energy Research Corporation, General Electric Company, New York State Energy Research and Development Authority, Northeast Utilities Service Company, Southern California Edison Company, The Standard Oil Company, and University of Rochester. Such support does not imply endorsement of the content by any of the above parties.

REFERENCES

1. See for example: A. J. Alcock, C. DeMichelis, V. V. Korobkin, and M. C. Richardson, *Appl. Phys. Lett.* **14**, 145 (1969); H. A. Baldis and P. D. Corkum, *Phys. Rev. Lett.* **45**, 1260 (1980); O. Willi, P. T. Rumsby, and S. Sartang, *IEEE J. Quantum Electron.* **QE-17**, 1909 (1981); C. Joshi, C. E. Clayton, A. Yasuda, and F. F. Chen, *J. Appl. Phys.* **53**, 215 (1982).

2. See for example: S. A. Akhmanov, A. P. Sukhorukov, and R. V. Khokhlov, *Sov. Phys. Usp.* **10**, 609 (1968); F. W. Perkins and E. J. Valeo, *Phys. Rev. Lett.* **32**, 1234 (1974); D. Anderson and M. Bonnedal, *Phys. Fluids* **22**, 105 (1979); D. Subbarao and M. S. Sodha, *J. Appl. Phys.* **50**, 4604 (1979); A. Schmitt and R. S. B. Ong, *J. Appl. Phys.* **54**, 3003 (1983); M. J. Giles, *J. Plasma Phys.* **29**, 325 (1983).
3. M. D. Feit and J. A. Fleck, *Appl. Phys. Lett.* **28**, 121 (1976).
4. R. C. Malone, R. L. McCrory, and R. L. Morse, *Phys. Rev. Lett.* **34**, 721 (1975).
5. R. S. Craxton and R. L. McCrory, Laboratory for Laser Energetics Report No. 108 (1980).
6. LLE Review **16**, 26 (1983).
7. M. Born and E. Wolf, *Principles of Optics*, 5th ed. (Pergamon Press, Oxford, 1975), p. 122.
8. J. H. Gardner *et al.*, Paper M5, 13th Annual Anomalous Absorption Conference, Banff, Alberta, Canada (1983).
9. J. A. Stamper *et al.*, Paper M6, 13th Annual Anomalous Absorption Conference, Banff, Alberta, Canada (1983).
10. S. Skupsky and K. Lee, *J. Appl. Phys.* **54**, 3662 (1983).
11. R. S. Craxton and R. L. McCrory, *J. Appl. Phys.* (to be published).

Section 3
ADVANCED TECHNOLOGY DEVELOPMENTS

3.A Time-Dependent Semiclassical Theory of Gain-Coupled Distributed Feedback Lasers

Recent interest in the transient behavior of distributed feedback lasers (DFL) has created the need for a more complete theoretical analysis than has existed previously. The photon rate equation model used by Zs. Bor[1] treats the time dependence of the laser output, but due to the mean field approximation inherent in this theory it is unable to treat the regime where spatial propagation and cavity length become important in determining the output pulse duration. This regime is of particular interest because of the possibility of producing single pulses of picosecond duration from such lasers.

The fundamental characteristic of a distributed feedback laser is that in the absence of external mirrors, the necessary feedback is provided by Bragg scattering from spatially periodic variations of the complex refractive index of the laser medium. This can be either the real component or the imaginary component (gain) of the material index or the effective index (as in an optical waveguide). In the case where the gain is used to vary the complex index, a nonlinear coupling occurs between the gain and the optical field. As the light intensity in the excited region increases, the gain is depleted, destroying the feedback and allowing the light to escape the medium. This self cavity-dumping can, for a range of pump energies, produce a train of ultrashort pulses. Typically these pulses are 50-100 times shorter than the pump pulse used.[2]

Semiclassical Theory of DFL

As in the rate equation theory,[1] the gain medium is modeled according to Fig. 18.21. Following the approach of Sargent *et al.*,[3] the system is described by the equations for the density matrix:

$$\dot{\rho}_{11} = -\gamma_{10}\rho_{11} + \gamma_{21}\rho_{22} + \left(\frac{i}{\hbar} V_{21}\rho_{12} + \text{c.c.}\right) \tag{1a}$$

$$\dot{\rho}_{22} = \lambda_2 - \gamma_{21}\rho_{22} - \left(\frac{i}{\hbar} V_{21}\rho_{12} + \text{c.c.}\right) \tag{1b}$$

$$\dot{\rho}_{21} = -(i\omega_o + \gamma)\,\rho_{21} + \frac{i}{\hbar} V_{21}\,(\rho_{22} - \rho_{11}). \tag{1c}$$

Note that ρ_{ii} is the population of level i, and γ is the homogeneous linewidth of the lasing transition. $V_{21} = -pE(z,t)$ is the atomic interaction energy, p is the dipole matrix element, and $E(z,t) = \frac{1}{2}[A(z,t)\exp(i\omega t) + \text{c.c.}]$ is the electric field in terms of the slowly varying envelope A(z,t). Here c.c. denotes the complex conjugate.

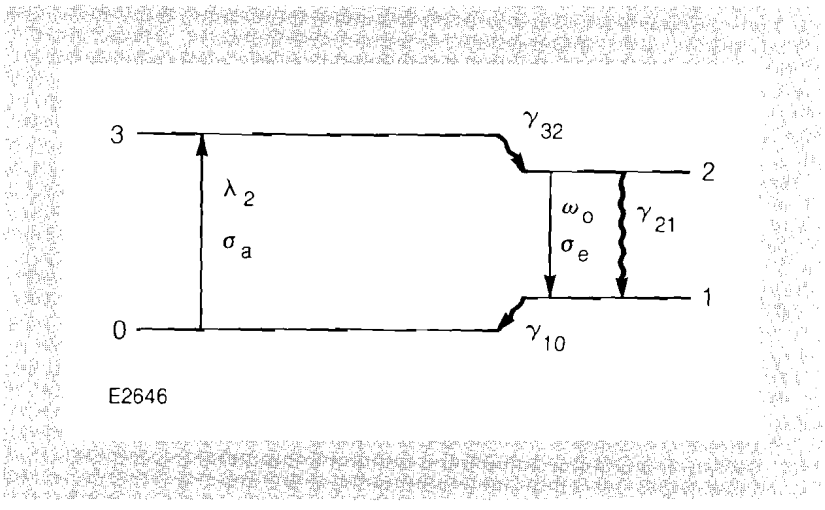

Fig. 18.21
The four-level system used for both the photon and semiclassical rate equations. The decay rates γ_{32} and γ_{10} are assumed to be large.

The density-matrix equations can be simplified by making the rate equation approximation for the gain medium (not the fields), which is valid when the linewidth γ is sufficiently large.[3,4] After formally integrating Eq. (1c) and assuming that A(z,t) and the population inversion $w(z,t) \equiv \rho_{22} - \rho_{11}$ vary little in time, γ^{-1}, ρ_{21} becomes approximately

$$\rho_{21} = \frac{-ip}{2\hbar}\,\frac{A^* w}{i\Delta + \gamma}\,e^{-i\omega t} \tag{2}$$

where $\Delta = \omega_o - \omega$ and nonresonant terms have been neglected (rotating wave approximation[5]). Substituting Eq. (2) into Eqs. (1a) and (1b) leads to

$$\dot{\rho}_{22} = \lambda_2 - \gamma_{21}\rho_{22} - \frac{p^2}{2\hbar^2}\,\frac{\gamma}{\Delta^2 + \gamma^2}\,|A|^2 w \tag{3a}$$

$$\dot{\rho}_{11} = \gamma_{21}\rho_{22} - \gamma_{10}\rho_{11} + \frac{p^2}{2\hbar^2}\,\frac{\gamma}{\Delta^2 + \gamma^2}\,|A|^2 w. \tag{3b}$$

The equations are further simplified by assuming that γ_{10} is large so that $\rho_{11} \ll \rho_{22}$ and $w \simeq \rho_{22}$. Then the inversion w obeys

$$\dot{w} = \lambda_2 - \gamma_{21}\, w - B\,|A|^2 w \tag{4}$$

where

$$B = \frac{p^2}{2\hbar}\left(\frac{\gamma}{\Delta^2 + \gamma^2}\right).$$

To provide feedback for the gain-coupled DFL the pumping rate λ_2 is spatially modulated with a period $\Lambda = \pi/\beta_0$,

$$\lambda_2 = N\lambda(t)\,(1 + V \cos 2\beta_0 z)$$

where, again, V is the visibility of the fringes and where $\lambda(t)$ accounts for the time dependence of the pumping, which may be provided by a laser pulse. To remove the rapid spatial modulation from the equations, and to go to a macroscopic description, a new inversion density variable W is defined by

$$W = \frac{Nw}{1 + V \cos 2\beta_0 z}\,. \tag{5}$$

The equation for the time dependence of W is then, from Eq. (4),

$$\dot{W} = N\lambda - \gamma_{21}\, W - B\,|A|^2 W. \tag{6}$$

The field evolution is determined by the wave equation,

$$\left[\frac{\delta^2}{\delta z^2} - \frac{n^2}{c^2}\,\frac{\delta^2}{\delta t^2}\right] E(z,t) = \frac{4\pi n^2}{c^2}\,\frac{\delta^2}{\delta t^2}\,P(z,t) \tag{7}$$

where the polarization $P = \frac{1}{2}\,[P(z,t)\exp(i\omega t) + \text{c.c.}]$.

If A(z,t) is separated into two counter-propagating waves

$$A(z,t) = Re^{i\beta_0 z} + Se^{-i\beta_0 z} \tag{8}$$

and substituted into Eq. (7) we obtain (ignoring second derivatives of R and S as well as the first derivative of P)

$$\left[i\beta_0 R' - \frac{1}{2}\left(\beta_0^2 - \frac{\omega^2 n^2}{c^2}\right)R - \frac{i\omega n^2}{c^2}\,\dot{R}\right] e^{+i\beta_0 z}$$

$$-\left[-\,i\beta_0 S' - \frac{1}{2}\left(\beta_0^2 - \frac{\omega^2 n^2}{c^2}\right)S + \frac{i\omega n^2}{c^2}\,\dot{S}\right] e^{-i\beta_0 z} = \frac{2\pi n^2 \omega^2}{c^2}\,P \tag{9}$$

where a prime (e.g., R′) indicates a partial derivative with respect to z. In the semiclassical theory the polarization is determined by

$$P = 2Np\,\rho_{12} e^{-i\omega_0 t}. \tag{10}$$

Using the value of $\rho_{12} = \rho_{21}^*$ from Eq. (2) we get

$$P = -\frac{iNp^2}{\hbar}\frac{Aw}{i\Delta+\gamma} . \tag{11}$$

Significant feedback occurs only for $\beta \simeq \beta_0$. Using this fact and Eq. (11), Eq. (9) can be separated into the following two equations:

$$R' - \frac{n}{c}\dot{R} + (\alpha W - i\delta)\, R = -\frac{\alpha V W}{2}\, S \tag{12a}$$

$$-S' - \frac{n}{c}\dot{S} + (\alpha W - i\delta)\, S = -\frac{\alpha V W}{2}\, R \tag{12b}$$

where $\delta = (\beta^2 - \beta_0^2)/2\beta_0$ and $\alpha = 2\pi\beta Np^2/\hbar(i\Delta+\gamma)$. Equations (12a) and (12b) were obtained by neglecting terms in $\exp(\pm i3\beta_0 z)$, i.e., by assuming that W is slowly varying spatially. This neglects spatial hole burning, which has been found to be relatively unimportant, in agreement with the steady-state case.[3]

Depletion of the ground state, level 0, is accounted for in the normal manner through the pump term $\lambda(t)$, i.e., by replacing

$$\lambda N \rightarrow \lambda(N-W). \tag{13}$$

In order to simulate spontaneous emission, a uniform noise term equivalent to one photon in the excited region was introduced into the field equations. The time-averaged energy is

$$\overline{\int_{V_0} \frac{E_0^2}{4\pi} dV} = \hbar\omega_0 .$$

where the integral is over the volume V_0 of the excited region. Assuming the noise to be equal in both directions, we find for the noise fields

$$R_0 = S_0 = \sqrt{\frac{4\pi\hbar\omega_0}{V_0}} . \tag{14}$$

The final equations are then,

$$R' - \frac{n}{c}\dot{R} + (\alpha W - i\delta)\,(R+R_0) = -\frac{\alpha W V}{2}\, S \tag{15a}$$

$$-S' - \frac{n}{c}\dot{S} + (\alpha W - i\delta)\,(S+S_0) = -\frac{\alpha W V}{2}\, R \tag{15b}$$

$$\dot{W} = \lambda(N-W) - \gamma_{21}\, W - B\,(|R|^2 + |S|^2)W. \tag{15c}$$

In going from Eq. (6) to Eq. (15c) the cross terms of $|A|^2$ were neglected, consistent with the assumption of no spatial hole burning.

DFL Calculations

Equations (15a), (15b), and (15c) were solved numerically. Due to the counter-propagating nature of the field solutions a second-order Euler method was used which required a square integration grid ($\Delta z = c\Delta t$). The equations were integrated subject to the boundary conditions that $S(L,t) = R(0,t) = W(z,0) = 0$, and that $\lambda(t)$ be Gaussian in time and uniform in space.

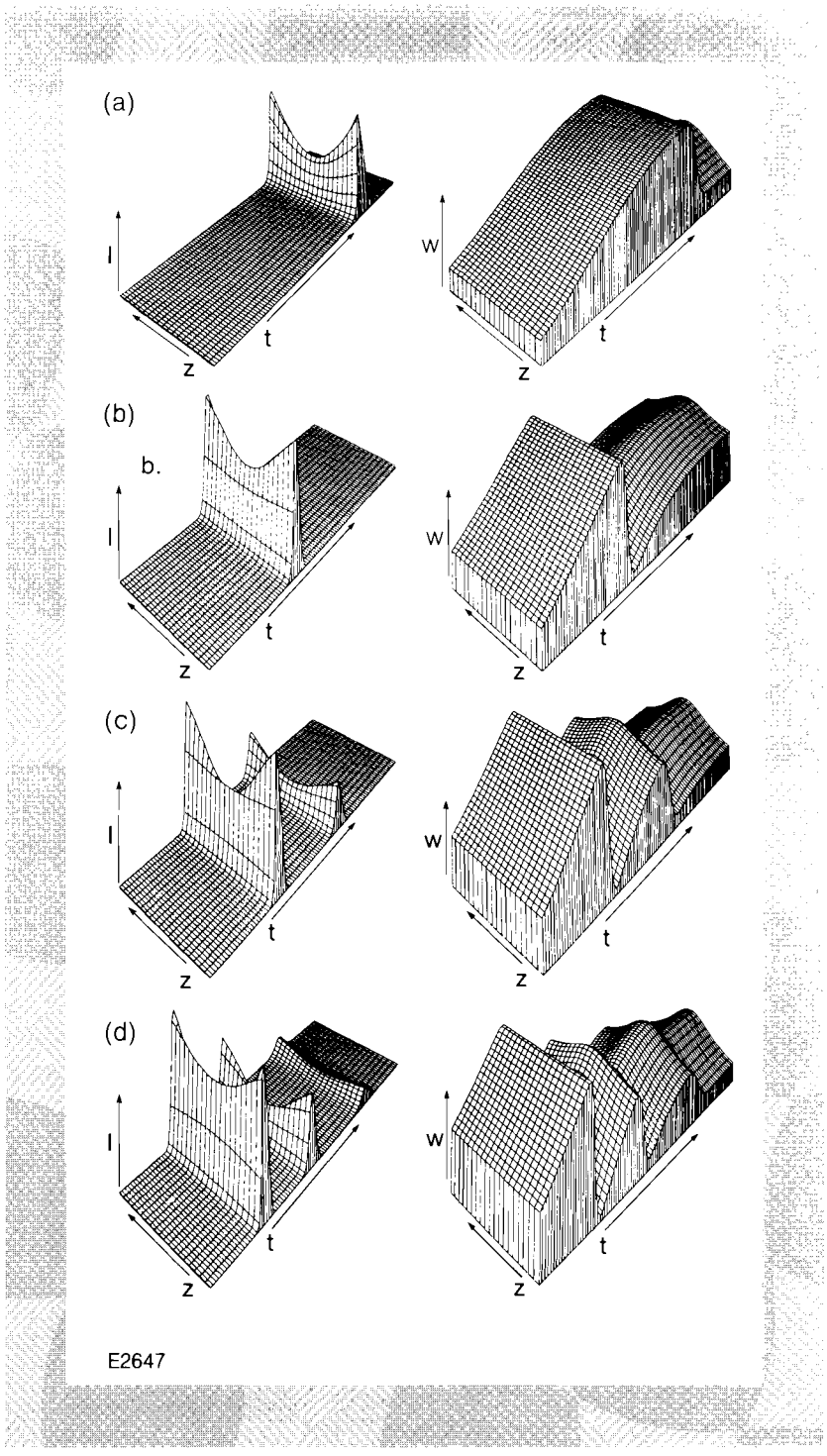

Fig. 18.22
Total intensity $I = R^2 + S^2$ and population inversion density W plotted as functions of time and space for an increasing pump energy. The pump-pulse duration was 70 ps, and the pumped region was 0.1 cm in length. The relative values of the pump energies are (a) 0.5, (b) 1.1, (c) 1.5, and (d) 2.0. The vertical scales are normalized, and the time axis represents 120-ps full scale.

The system parameters were chosen appropriate for Rhodamine 6G in ethylene glycol as the active medium in the distributed feedback laser, i.e., $N = 3.5\times10^{-3}$ M (2.1×10^{18} mol/cm^2), $V_0 = bL/N\sigma_a$, $b = 0.025$ cm, $\sigma_a = 2.7\times10^{-16}$cm^2, $\alpha = \sigma_e/2$, $\sigma_e = 1.4\times10^{-16}$cm^2, $\tau = 1/\gamma_{21} = 4$ ns, $V = 1.0$, $n = 1.44$.

Due to the nonlinear coupling between the gain, the Bragg reflectivity, and the field, a self cavity-dumping is observed for a range of pump energies in the DFL. The inversion builds up as the integral of the pump pulse until the field increases sufficiently for gain saturation to become dominant. At this time, the Bragg reflectivity decreases rapidly allowing the field to escape as a pulse. If this process occurs during the pump pulse, the inversion has the opportunity to recover and produce a second pulse. As the pump energy is increased, the initial dumping will occur at earlier times allowing additional pulses to be produced. In Fig. 18.22, the total intensity $I = R^2 + S^2$ and population inversion W are shown for a sequence of increasing pump energies. The solutions are plotted as functions of space and time. The laser output is directly proportional to the value of the total intensity at the end face ($z = 0,L$) of the pumped region. The behavior of these solutions at the end faces is in very close qualitative agreement with the photon rate equation model.[1]

Using the previously published predictions[6] of the photon rate equations for the duration of the initial output pulse as a function of the length of the pumped region given that either (a) the second pulse is at threshold or (b) the third pulse is at threshold, the new theory can be quantitatively evaluated as to its performance in the limit of long pump pulses, $T_p \gg nL/c$. This comparison is shown in Fig. 18.23 for a pump pulse of 3.5 ns. The results show excellent agreement between the two theories in this limit. It is interesting to note that, although there is an offset, the slope of the dependence is very close to that of the line $t = nL/c$.

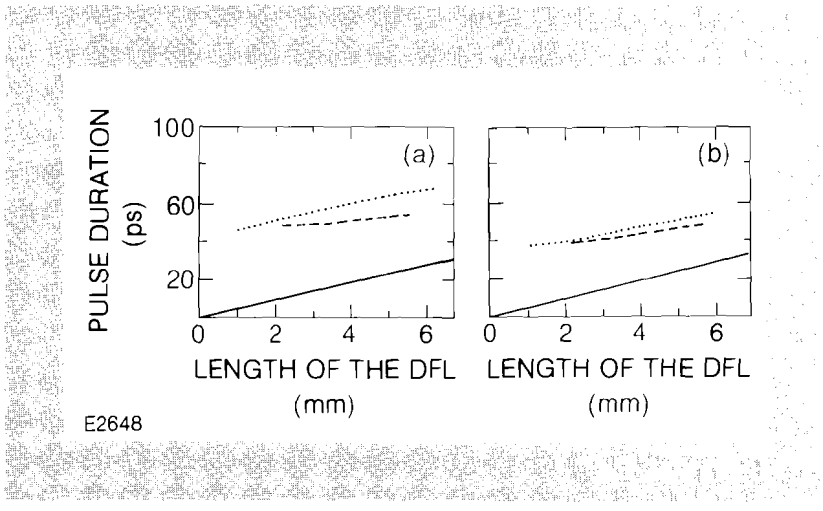

Fig. 18.23
Duration of the first pulse as a function of the length of the DFL for a 3.5-ns pump pulse and (a) the second pulse at threshold, and (b) the third pulse at threshold. The dashed line corresponds to the photon rate equation prediction, and the dotted line to the semiclassical prediction. The solid line is $t = nL/c$.

It has been shown previously that as the pump pulse width is reduced, the pulse duration of the DFL will also shorten.[2] However, as the pump pulse duration becomes comparable to the pumped-region transit time ($T_p = nL/c$) the photon rate equation analysis will be

invalid. In Fig. 18.24, the predicted pulse width versus pumped-region length [similar to Fig. 18.23(a)] in the case of a 70-ps pump pulse is shown for the two theories. Again, the line t=nL/c is shown. A large discrepancy between the theories is evident which, as expected, decreases as the length of the pumped region is decreased. It is seen that the pulse widths are much longer than predicted by the photon rate equations and that their duration approaches the transit time nL/c.

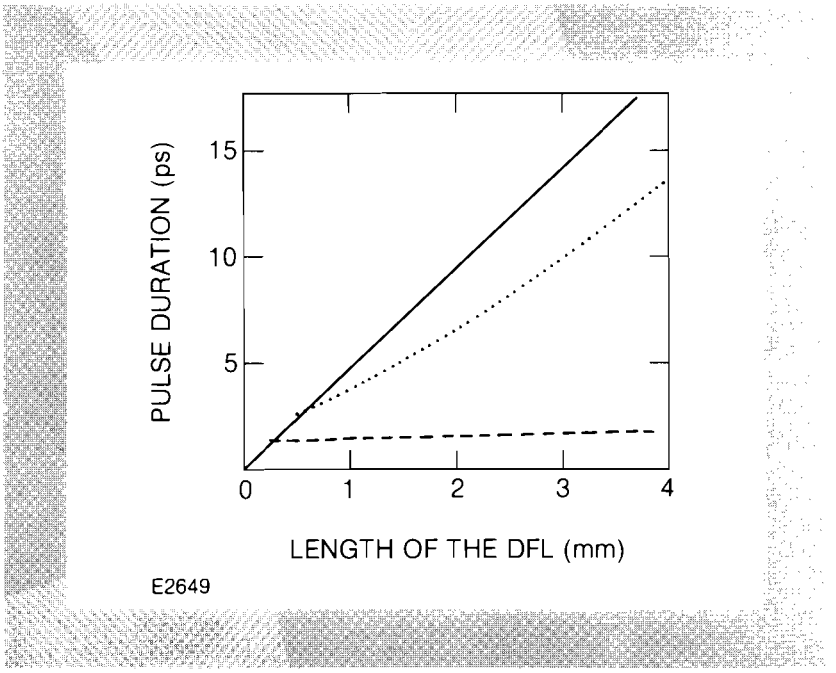

Fig. 18.24
Duration of the first pulse as a function of the length of the DFL for a 70-ps pump pulse and the second pulse at threshold. The dashed line is that predicted by the photon rate equation model, and the dotted line is that predicted by the semiclassical theory. The solid line is t = nL/c.

In the steady-state limit, $\dot{S} = \dot{R} = 0$, the field equations (12) reduce directly to the form of previous steady-state theories[3,7] in the gain-coupled case. The amount of Bragg reflectivity at any point is proportional to the coefficient of the coupling term in the field equations. The value of this coupling coefficient determines the nature of the field distribution. For a gain-coupled laser, the coupling coefficient can be expressed as αVWL/2. It has been shown in the steady-state analyses that if $\alpha VWL/2 < 1.5$, termed undercoupled, the field distribution will be peaked toward the ends of the pumped region, while if $\alpha VWL/2 > 1.5$, termed overcoupled, the distribution will be peaked in the center of the cavity. In the case of steady-state pumping shown in Fig. 18.25, after the initial oscillations damp out, the coupling coefficient can be calculated for different positions in the pumped region. The coupling coefficient varies from 0.42 at the edge of the region (z = 0,L) to 1.3 in the center (z = L/2) where it is at a maximum. This evaluation agrees with the form of the intensity distribution seen in Fig. 18.25(c), which shows behavior typical of undercoupling.

We have found that due to gain saturation in a laser of this type, the high values of αVWL required for overcoupled operation cannot be maintained in the steady state. However, during the transient field build-up, prior to gain saturation, the coupling coefficient can reach values in the overcoupled range. This results from the gain over-

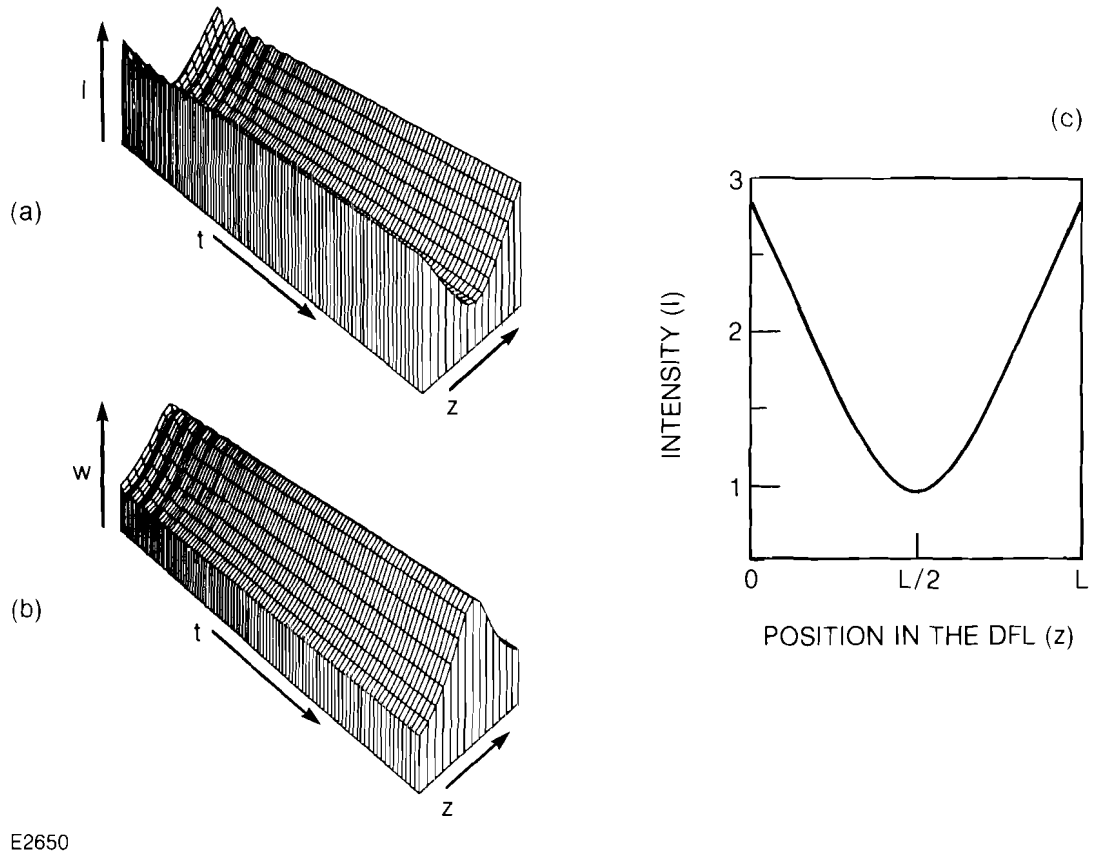

Fig. 18.25
The intensity I and inversion density W as functions of space and time for steady-state pumping (a, b) and the final intensity distribution along the length of the DFL (c). The length of the DFL was 0.3 cm.

shooting the steady-state value prior to the field build-up. As the field builds up, it experiences strong coupling and, therefore, peaks in the center of the cavity. Then, as the transient field depletes the gain, the laser shifts to the undercoupled regime enabling the pulse to escape. In Fig. 18.26, 3-D plots of two cases are shown. For each case the plot is viewed both from earlier times [Figs. 18.26(a) and 18.26(c)] , and from later times [Figs.18.26(b) and 18.26(d)] to allow examination of the intensity distribution as it evolves. In Fig. 18.26(a), the contours of equal time can be seen to have positive curvature indicating an overcoupled intensity distribution, while at later times [Fig. 18.26(b)], the contours show the negative curvature typical of undercoupled operation. Figures 18.26(c) and 18.26(d) are the same views of the field when the pumped region is made shorter. In this case the operation is undercoupled ($\alpha VWL/2 < 1.5$) even during the buildup, as seen by negative curvatures at all times.

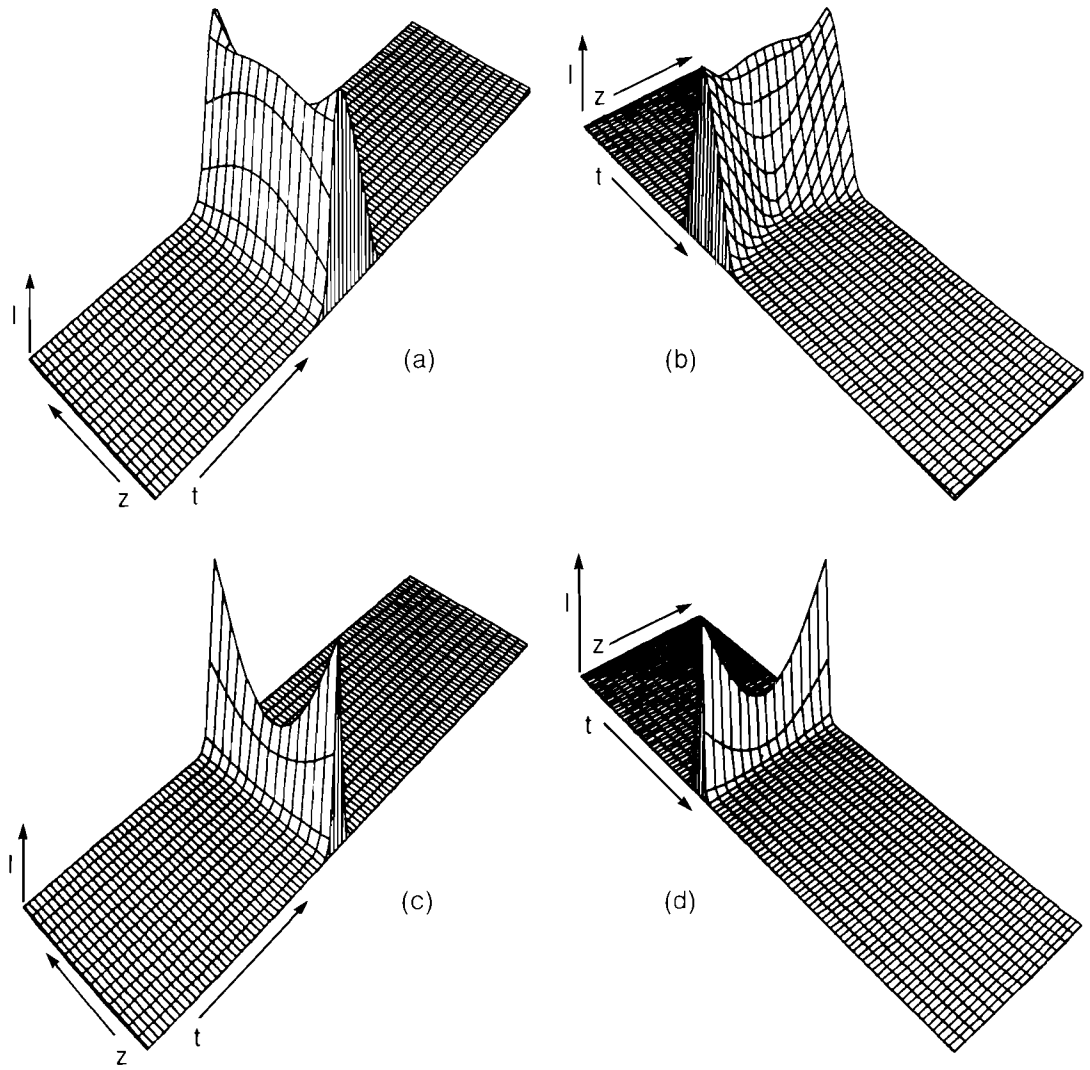

Fig. 18.26
The intensity as functions of space and time for the case of the DFL of length 0.3 cm (a, b) and 0.03 cm (c, d). In both cases the pump intensity was adjusted so that the second pulse was at threshold. For each case the intensity distribution is shown as seen from earlier times (a, c) or from later times (b, d).

Conclusion

Due to the inability of the photon rate equation analysis of the DFL to predict the output characteristics accurately in the regime where the pumped-region transit time is comparable to the pump pulse length, a semiclassical treatment has been developed which takes into account the spatial variation of the field and inversion along the pumped region. The addition of this consideration provides a theory capable of handling both the short-time transient regime and the

steady-state limit. Comparisons with existing transient and steady-state theories show close agreement in the limits where those theories are valid, and predictions are made in the short-pulse regime where the photon rate equation is invalid. These predictions indicate that the pulse duration is dominated by the transit time along the pumped region. Also, a careful evaluation of the field evolution shows that in some cases the laser is overcoupled at early times and, as the pulse is emitted, becomes undercoupled; in other cases the operation remains undercoupled throughout the buildup and pulse emission process. This provides new insight into the mechanisms involved in the DFL. Further refinements of this theory which may have an effect on the output characteristics will include excited state absorption, reabsorption of the lasing light in the case of dye lasers, molecular rotation and diffusion, and the addition of a saturable absorber to the medium.

ACKNOWLEDGMENT

This work was supported by the following sponsors of the Laser Fusion Feasibility Project at the Laboratory for Laser Energetics—Empire State Electric Energy Research Corporation, General Electric Company, New York State Energy Research and Development Authority, Northeast Utilities Service Company, Southern California Edison Company, The Standard Oil Company, and University of Rochester. Such support does not imply endorsement of the content by any of the above parties.

REFERENCES

1. Zs. Bor, *IEEE J. Quantum Electron.* **QE-16**, 517 (1980).
2. G. Szabo, Zs. Bor, and A. Muller, *Appl. Phys. B* **31**, 1 (1983).
3. M. Sargent, W. H. Swantner, and J. D. Thomas, *IEEE J. Quantum Electron.* **QE-16**, 465 (1980).
4. L. Allen and J. H. Eberly, *Optical Resonance and Two Level Atoms* (John Wiley and Sons, New York, 1975) p. 134.
5. *Op. cit.*, p. 28.
6. Zs. Bor, A. Muller, B. Racz, and F. P. Schafer, *Appl. Phys. B* **27**, 9 (1982).
7. H. Kogelnik and C. V. Shank, *J. Appl. Phys.* **43**, 2327 (1972).

3.B Pulse Shaping with Dispersive Microstriplines

Laser-driven inertial-fusion targets require carefully controlled temporal shaping of the driver pulse to achieve high performance. Saturation during propagation of the beam through many stages of amplification results in the need to shape the input pulse in order to attain the required output temporal shape. A particularly effective method of shaping the input optical pulse involves the production of specific electrical waveforms which can be synchronized with a square optical pulse, in an electro-optic crystal, to create a shaped optical pulse. These electrical transients have been generated using a frozen wave generator developed at LLE[1] and a tapered-line pulse shaper proposed at LLNL.[2] These methods rely on multiple reflections

within transmission-line elements to create the desired waveforms, and, thus, are more complicated to use than a method which employs the dispersive properties of a transmission line near its cut-off frequency. These dispersive properties have been predicted by G. Hasnain *et al.*[3] and observed by Valdmanis, Mourou, and Gabel[4] in the picosecond and subpicosecond range. We have developed a technique that uses dispersion to generate monotonically increasing high-voltage waveforms in the nanosecond and subnanosecond timescales which are required for laser fusion. The result of the design, construction, and operation of a dispersive two-conductor transmission line is compared with calculations which simulate the evolution of the actual input pulses along this line.

Experimental Investigations

Our investigation of pulse shaping utilizes the intrinsically dispersive microstrip transmission line, which demonstrates frequency-dependent propagation velocities due to the conveyance of non-TEM modes. The dielectric substrate and the air superstrate create an inhomogeneous dielectric geometry, and the microstrip exhibits a discontinuity in the field lines between its strip and ground plane. This field configuration can be shown, through simple arguments based on Maxwell's equations, to contain the longitudinal components producing dispersion. Since we wish to create rather than avoid dispersed waveforms, it is convenient to maximize the effect of those parameters which most influence the field discontinuities. This indicates that the high-frequency relative dielectric constant and thickness of the substrate should both be made large. Characteristic impedance limitations require that a thick substrate be matched with a wide stripline, and, thus, our microstrip is designed with a large geometry, restricted mainly by the availability of thick substrates of substantial high-frequency dielectric constant.

The complete pulse shaping system is shown in Fig. 18.27. The input electrical pulse is generated with the use of a semiconductor photoconductive switch, which acts as a gate to a dc-biased charge line. This switch is closed when driven by a single, high-intensity, 100-ps optical pulse (1064 or 532 nm) from a cw-pumped, q-switched, mode-locked Nd:YAG oscillator. The output pulse from the switch follows the laser pulse and exhibits a rise time of about 100 ps; the pulse duration is determined by the natural recombination of the semiconductor or the length of the charge line. The most important characteristic of this pulse is its rising edge, which contains high-frequency components up to 3.5 GHz. As long as the cut-off frequency of a microstrip is below this frequency, dispersion will occur and the original shape of the pulse will change.

The microstrip, to which the switch output pulse is coupled, consists of a thick piece of acrylic, situated between two copper foil electrodes. In this instance, the copper electrodes are placed in the configuration used for previous work,[5] that of a balanced microstrip. This geometry utilizes two electrodes of equal width, rather than having one as a ground plane with the dimensions of the substrate; it also serves to reduce the effective substrate height to half the value of a conventional

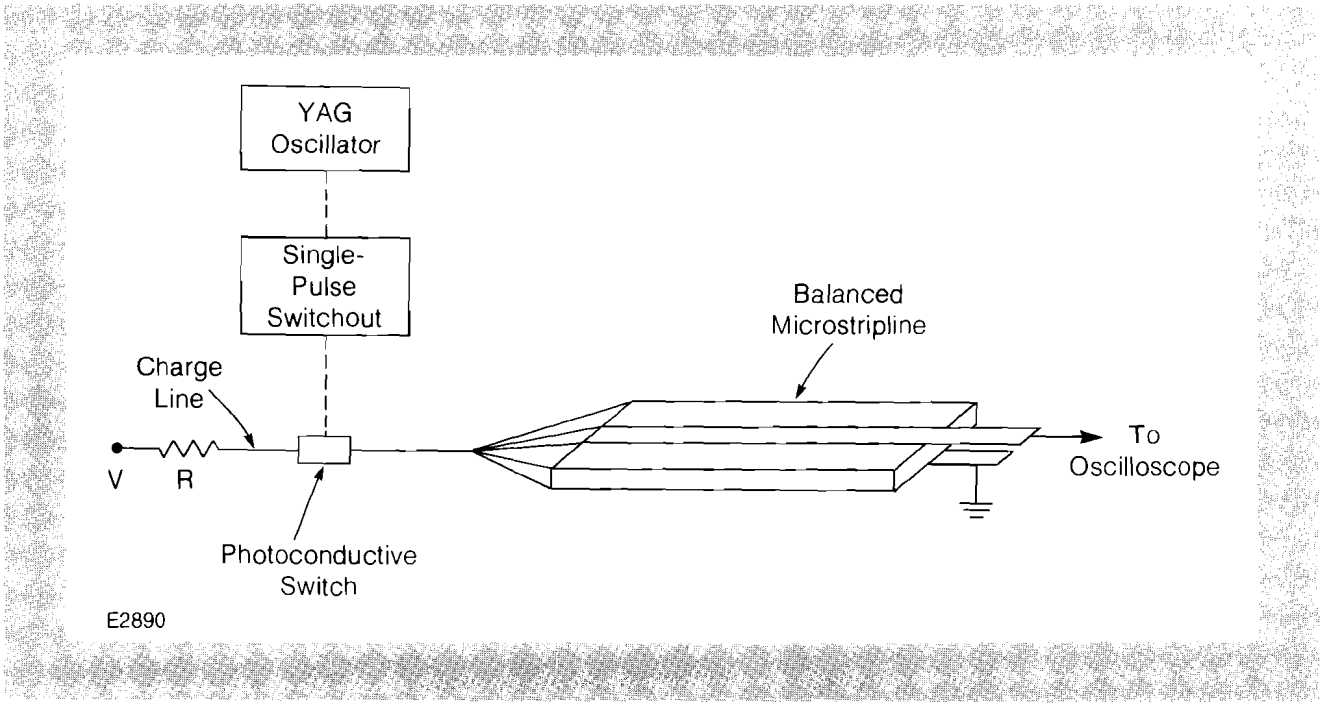

Fig. 18.27
Schematic diagram of the dispersive transmission line pulse shaper. A section of cable is discharged through a semiconductor photoconductive switch driven by a single 100-ps pulse from a q-switched, mode-locked Nd:YAG oscillator. The switch output is coupled to a balanced microstrip which has a cut-off frequency below that corresponding to the input-pulse rise time. The pulse shape at the output of the line is reconstructed with a sampling oscilloscope.

microstrip. However, reducing the height, as mentioned earlier, also reduces the dispersion, so that all follow-up experiments have been conducted using a stripline with a ground plane.

The substrate is cut into several segments, each of different length, so that the dispersion can be observed as a function of propagation distance along the line. The dispersed output pulse is reconstructed using a Tektronix S-6 sampling head mounted in a 7834 mainframe. The dispersion is evidenced in the sampled waveforms through the delay of high-frequency information with respect to that of low frequency. As the waveform is sampled at greater propagation distances, the high frequencies are delayed by greater amounts. Therefore, the rise time consists of lower frequencies and becomes longer. In addition, as the high-frequency components are delayed through the rest of the pulse, a pulse-sharpening effect attributed to energy conservation becomes apparent, and a secondary pulse which grows with propagation distance is formed. The progress of the dispersed pulse is outlined in Fig. 18.28.

Theoretical Calculations

These observations are supported by the results of calculations which simulate the evolution of the experimental input pulse along a microstrip (see Fig. 18.28). The rise times and FWHM durations are compared with the estimated values from the observed waveforms. The rise times of the experimental and calculated pulses consistently agree to within the resolution on our sampling oscilloscope. The simulation also predicts the formation of the secondary pulse and the increase in the pulse width with propagation distance. Some of the discrepancies in waveform shapes may be attributed to reflections due to characteristic impedance mismatches when coupling signals between a switch, coaxial cable, and the microstrip.

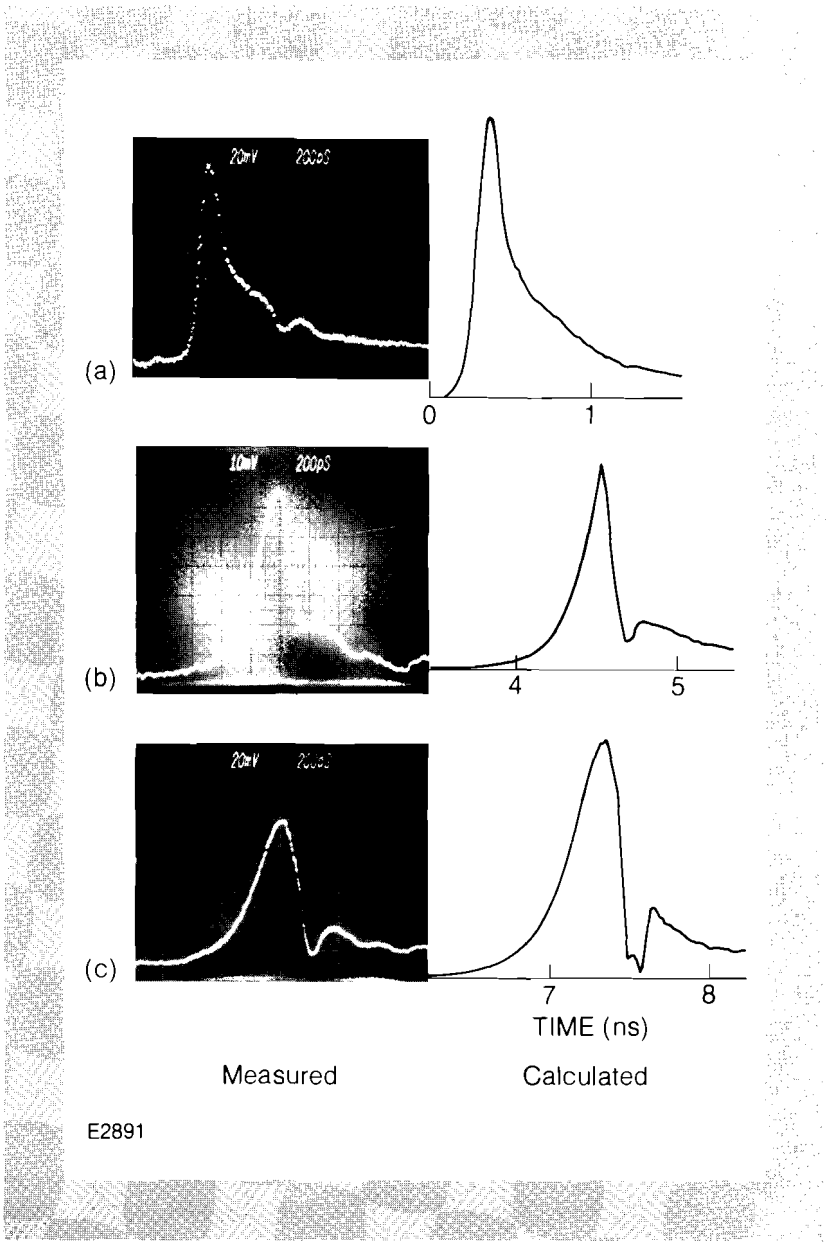

Fig. 18.28.
Comparison of experimental and calculated pulses propagating on a microstripline.

- *(a) The real and digitized switch output/microstrip input pulse.*
- *(b) Dispersed pulse after 82.1 cm of travel on microstrip. Experimentally, the 10-90% rise time is 320 ps. Theoretically, it is 350 ps.*
- *(c) Dispersed pulse after 137.7 cm of propagation. Experimentally, the rise time is 400 ps. Theoretically, it is 415 ps.*

The simulation of this dispersion is accomplished by first reading into the computer the normalized values corresponding to the experimental input pulse, along with the relevant parameters of the substrate: geometry, conductivity, and high- and low-frequency dielectric constants; and the parameters of the strip-conductor: geometry and resistivity. The spectrum of the input pulse is then multiplied by the complex propagation factor of the striplines with frequency-dependent phase and attenuation terms, before a final transformation is made to return the pulse to the time domain. It should be noted that the theory employed here is by no means exact. Both the functions used to determine the frequency-dependent relative and effective dielectric constants of the substrate (the latter is derived by curve-fitting to the exact analysis[6]) are simple approximate formulae, so that, depending on the properties of the substrate involved, the accuracy will vary.

The dependability with which predictions of pulse shapes can be made indicates that stripline materials and geometries may be designed to yield specific waveforms for fusion applications. Typically, these waveforms consist of monotonically rising ramps with front-to-back contrast ratios of the order of 10:1 (see Fig. 18.29). This ramp is synchronized, in an electro-optic crystal, with a square optical pulse so that the resultant optical pulse has the same shape as the front ramp of the electrical pulse. Thus, the microstrip can be designed to exhibit its maximum dispersive capabilities; then the propagation length, input electrical transient duration, and synchronization between electrical and optical pulses are adjusted until the appropriate optical waveform is created.

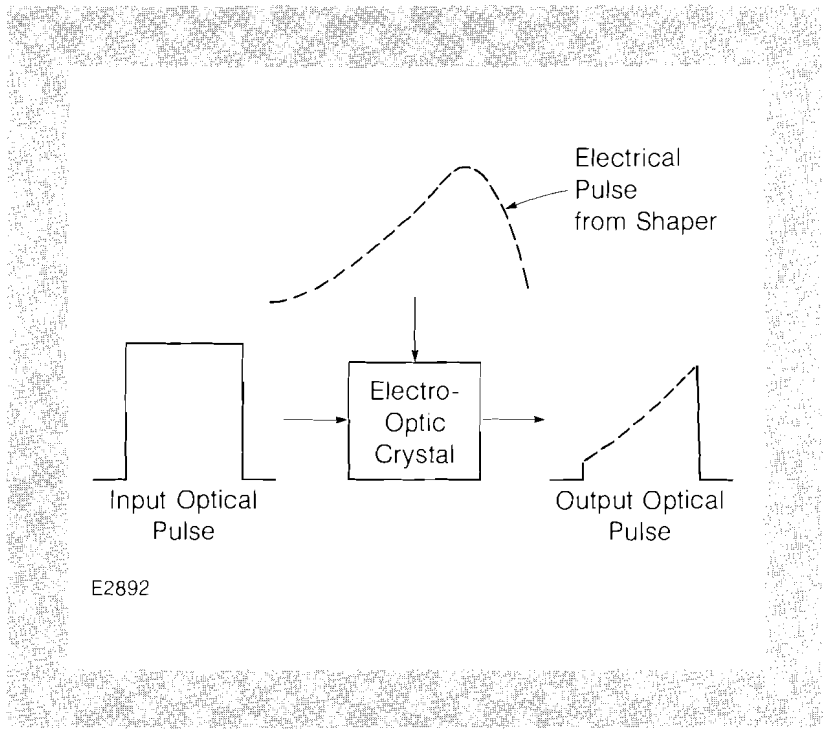

Fig. 18.29
Synchronization of a flat optical pulse with the rising edge of an electrical "shaper" pulse. The output optical pulse will exhibit the same gradual rise which is produced by dispersion of a fast pulse on a microstripline.

Conclusion

We have demonstrated that the concepts developed for the dispersion of picosecond pulses on microstrips apply also for longer pulses which are useful for laser fusion experiments. We also have a simple theory by means of which the shape of dispersed waveforms on microstrips can be accurately predicted. Finally, we have discussed a technique which exists for generating electrical pulses suitable for use in optical pulse-shaping projects.

ACKNOWLEDGMENT

This work was supported by the U.S. Department of Energy Office of Inertial Fusion under contract number DE-AC08-80DP40124 and by the Laser Fusion Feasibility Project at the Laboratory for Laser Energetics which has the following sponsors: Empire State Electric Energy Research Corporation, General Electric Company, New York State Energy Research and Development Authority, Northeast Utilities Service Company, Southern California Edison Company, The Standard Oil Company, and University of Rochester. Such support does not imply endorsement of the content by any of the above parties.

REFERENCES

1. J. Whitaker and D. Smith, report to the annual meeting of the Rochester chapter of the Electron Device Association of the IEEE, 1983.
2. R. Wilcox, Lawrence Livermore National Laboratory Report OPS 83-221, July 1983.
3. G. Hasnain, G. Arjavalingam, A. Dienes, and J. R. Whinnery, *Proc. SPIE Conference on Picosecond Opto-electronics, Vol. 439*, San Diego, 1983.
4. J. A. Valdmanis, G. A. Mourou, and C. W. Gabel, *IEEE J. Quantum Electron.*, **QE-19**, 664 (1983).
5. J. A. Valdmanis, Ph.D. thesis, University of Rochester, 1983.
6. E. Yamashita, K. Atsuki, and T. Ueda, *IEEE Trans. Microwave Theory Tech.*, **MTT-27**, 1036 (1979).

Section 4
NATIONAL LASER USERS FACILITY NEWS

This report covers the activities of the National Laser Users Facility (NLUF) during the quarter 1 January to 31 March 1984. During this period, one user conducted experiments on LLE facilities and another continued diagnostic development. Visiting scientists representing the Naval Research Laboratory (NRL) and the Goddard Space Flight Center (GSFC) performed experiments on the OMEGA facility, compiling a total of 17 shots. The University of Hawaii at Manoa initiated the installation of its spectrograph.

User Experiments

The user experiment on the OMEGA system used 351-nm laser light focused onto copper, zinc, and gallium targets. The XUV spectra is used to identify transitions in the 100–200-Å wavelength region. The NRL-GSFC 3-m spectrograph, already in place at LLE, was used for the identification of transitions from neon-like and nearby ionization stages. The participating individuals of this experiment are

- **Uri Feldman, George Doschek, John Seely,** and **Brian Dohne** (Naval Research Laboratory), and **W. E. Behring** (Goddard Space Flight Center): "Measurement of the Spectra of Neon-Like Ions Relevant to X-Ray Lasers Using the OMEGA Laser Facility."

A new streak camera/photographic camera coupled with an elliptical analyzer, x-ray spectrograph system (SPEAXS) is currently being installed on the OMEGA target chamber by an on-site investigator — Paul Jaanimagi. With the SPEAXS system, time-resolved and

absolutely calibrated, time-integrated x-ray spectra will be obtained from the laser-produced plasma. The available analyzer crystals range from lead behenate (2d spacing = 120 Å) to lithium fluoride (2d spacing = 4.027 Å) and will allow investigation of the x-ray emission in the 100-10,000-eV region. The participating individuals of this experiment are

- **Burton L. Henke** and **Paul A. Jaanimagi** (University of Hawaii at Manoa): "Evaluation and Application of a Streak Camera and Photographic Camera Coupled Elliptical-Analyzer Spectrograph System for the Diagnostics of Laser-Produced X-Ray Sources (100-10,000-eV Region)."

Additional information on these experiments can be obtained from the scientists associated with the experiment.

Steering Committee Meeting

On 20 April 1984, the NLUF Steering Committee will hold its fifth meeting to review and approve proposals, and to recommend funding of approved proposals in inertial fusion to the U.S. Department of Energy. This funding allocation is separate from LLE's operation contract and is designed to provide research funds to users in the inertial fusion field. Users in other fields may use the facility, but must provide their own research funds.

The committee membership consists of

Brian J. Thompson, Chairman
(Dean, College of Engineering & Applied Science, University of Rochester)

Thomas C. Bristow, non-voting Executive Secretary
(NLUF Manager)

John C. Browne
(Los Alamos National Laboratory)

Michael Campbell
(Lawrence Livermore National Laboratory)

Arthur H. Guenther
(Air Force Weapons Laboratory)

Wulf B. Kunkel
(Department of Physics, University of California at Berkeley)

Robert P. Madden
(National Bureau of Standards)

Barry H. Ripin
(Naval Research Laboratory)

Donald C. Slater
(KMS Fusion, Inc.)

Last year the committee approved 11 of the 22 submitted proposals. The next issue of the LLE Review will list the approved proposals for this coming year.

ACKNOWLEDGMENT

This work was supported by the U.S. Department of Energy Office of Inertial Fusion under contract number DE-AC08-80DP40124.

Further information on the NLUF is available by writing to:

Thomas C. Bristow, Manager
National Laser Users Facility
Laboratory for Laser Energetics
University of Rochester
250 East River Road
Rochester, New York 14623
(716) 275-2074

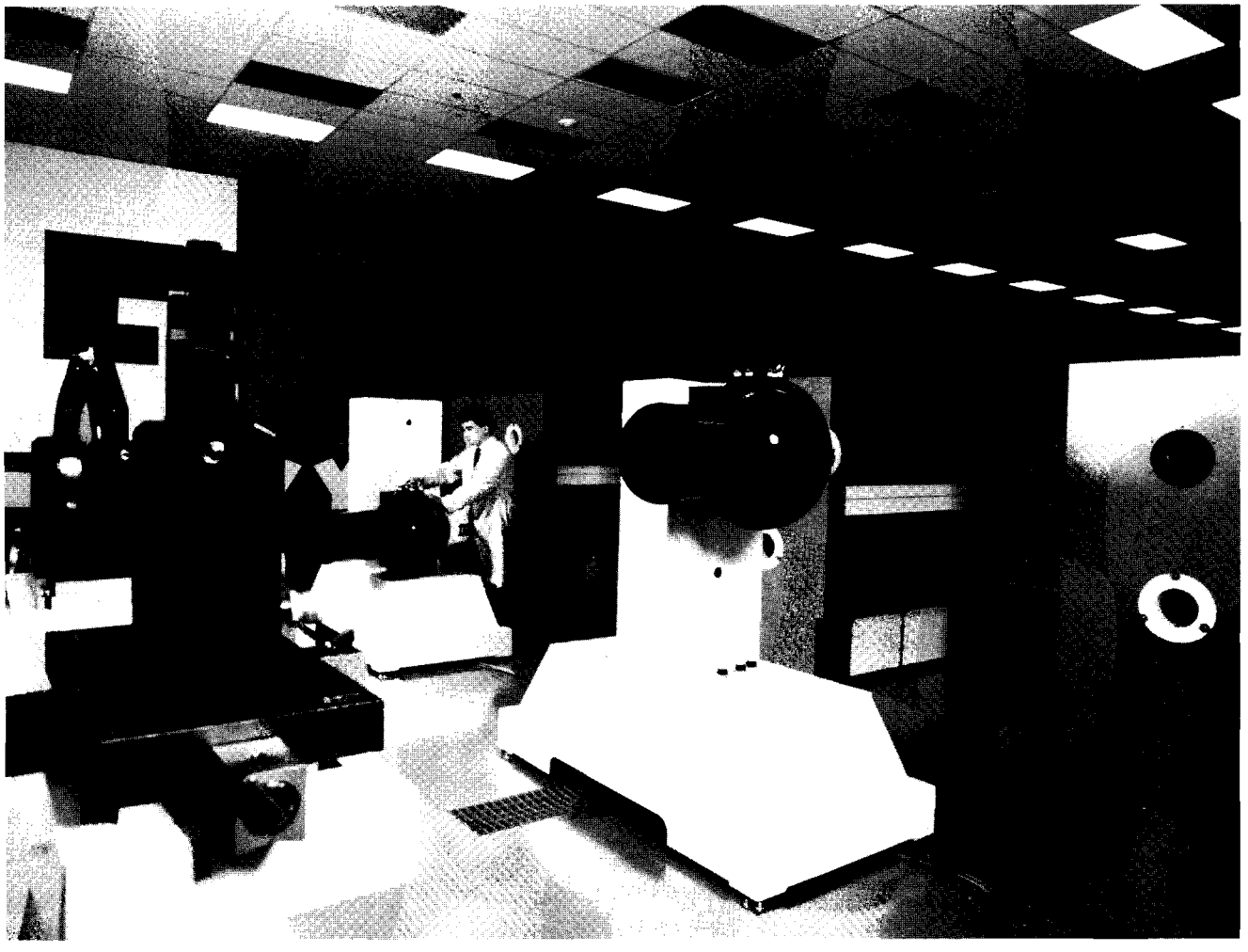

Gregory Pien, a technician in the OMEGA Operations Group, is shown aligning a multi-wavelength energy-sensing system (MESS) on one of the six OMEGA beams which have been converted to 351-nm operation. These devices measure the amount of energy at 1ω, 2ω, and 3ω in each of the converted beams. See the article on OMEGA energy measurement in this volume for additional information on these devices.

PUBLICATIONS

S. Skupsky, R. L. McCrory, R. S. Craxton, J. Delettrez, R. Epstein, K. Lee, and C. Verdon, "Uniformity of Energy Deposition for Laser-Driven Fusion," *Laser Interaction and Related Plasma Phenomena*, edited by H. Hora and G. Miley (Plenum Press, New York, 1984), p. 751.

B. A. Yaakobi, J. Delettrez, L. Goldman, R. L. McCrory, R. Marjoribanks, M. C. Richardson, D. Shvarts, S. Skupsky, J. M. Soures, C. Verdon, D. Villeneuve, T. Boehly, R. Hutchison, and S. Letzring, "Thermal Transport Measurements in 1.05 μm Laser Irradiation of Spherical Targets," *Phys. Fluids* **27**, 516 (1984).

M. C. Richardson, T. R. Boehly, B. A. Brinker, T. C. Bristow, R. S. Craxton, J. A. Delettrez, G. Enright, A. Entenberg, W. Friedman, L. M. Goldman, J. Hoose, R. J. Hutchison, L. Iwan, S. Kacenjar, K. Lee, S. A. Letzring, L. D. Lund, R. S. Marjoribanks, R. L. McCrory, J. M. Miller, J. Rizzo, W. D. Seka, S. Skupsky, J. M. Soures, C. P. Verdon, D. M. Villeneuve, E. A. Williams, and B. Yaakobi, "Progress Toward Direct Drive Laser Fusion," *Laser Interaction and Related Plasma Phenomena*, edited by H. Hora and G. Miley (Plenum Press, New York, 1984), p. 903.

B. Yaakobi, J. Delettrez, R. L. McCrory, R. Marjoribanks, M. C. Richardson, D. Shvarts, J. M. Soures, C. Verdon, D. M. Villeneuve, T. Boehly, R. Hutchison, and S. Letzring, "Thermal Transport Measurements in 1.05 μm Laser Irradiation of Spherical Targets," *Laser Interaction and Related Plasma Phenomena*, edited by H. Hora and G. Miley (Plenum Press, New York, 1984), p. 731.

B. Yaakobi and A. Burek, "Crystal Diffraction Systems for X-Ray Spectroscopy Imaging and Interferometry on Laser Fusion Targets," *IEEE J. Quantum Electron.* **QE-19**, 1841 (1983).

M. C. Richardson, R. Marjoribanks, S. Letzring, J. Forsyth, and D. Villeneuve, "Spectrally Discriminating Time-Resolved and Space-Resolved X-Ray Plasma Diagnostics," *IEEE J. Quantum Electron.* **QE-19**, 1861 (1983).

D. M. Villeneuve, R. Keck, B. Afeyan, W. Seka, and E. Williams, "Production of Hot Electrons by Two Plasmon Decay Instability in UV Laser Plasma," *Phys. Fluids*, **27**, 721 (1984).

J. A. Valdmanis, G. A. Mourou, and C. W. Gabel, "Picosecond and Subpicosecond Optoelectronics for Measurements of Future High Speed Electronic Devices," *Proceedings of the IEEE International Electron Devices Meeting*, December 1983.

Forthcoming Publications

R. W. Short, W. Seka, K. Tanaka, and E. A. Williams, "Two-Plasmon Decay and Three Halves Harmonic Generation in Filaments in a Laser Plasma," accepted for publication by *Physical Review Letters*.

E. L. Lindman and K. Swartz, "Some Applications of the Hot Electron Transport Equation," to be published in CECAM Workshop Report *The Flux Limiter and Heat Flow Instabilities in Laser-Fusion Plasmas* (1983).

H. Kim, T. Powers, and J. Mason, "Inertial Fusion Target Fabrication Using Polystyrene Mandrels," accepted for publication by *Journal of Vacuum Science and Technology*.

N. S. Murty and H. Kim, "Molecular Packing in Alkylated and Chlorinated Poly-p-paraxylylenes," accepted for publication by *Polymer*.

M. C. Richardson, S. Skupsky, J. Kelly, L. Iwan, R. Hutchison, R. Peck, R. L. McCrory, and J. M. Soures, "Laser Fusion Target Irradiation Uniformity with the 24-Beam OMEGA Facility," accepted for publication in *SPIE Volume 380, Proceedings of 1983 Los Alamos Conference on Optics*.

M. C. Richardson, S. A. Letzring, W. Friedman, and G. Gregory, "Time Resolved X-Ray Photography of Uniformly Irradiated Spherical Targets," accepted for publication in *SPIE Volume 427, Proceedings of the High-Speed Photography, Videography, and Phototonics*, San Diego, CA, 1983.

B. Yaakobi, H. Kim, and J. M. Soures, "Submicron X-Ray Lithography Using UV Laser Produced Plasma as a Source," accepted for publication by *1983 Proceedings of the American Vacuum Society Conference*.

R. S. Craxton and R. L. McCrory, "Hydrodynamics of Thermal Self-focusing in Laser Plasmas," accepted for publication by *Journal of Applied Physics*.

J. Abate, A. Schmid, M. Guardalben, D. Smith, and S. Jacobs, "Characterization of Micron-Sized, Optical Coating Defects by Photothermal Deflection Microscopy," accepted for publication in the *Proceedings of the 15th Annual Symposium on Optical Materials for High Powered Lasers*.

The work described in this volume includes current research at the Laboratory for Laser Energetics which is supported by Empire State Electric Energy Research Corporation, General Electric Company, New York State Energy Research and Development Authority, Northeast Utilities Service Company, Southern California Edison Company, The Standard Oil Company, University of Rochester, and the U.S. Department of Energy Office of Inertial Fusion under contract DE-AC08-80DP40124.